

OPTICAL SWITCHING CONTROLLER USING FPGA AS A CONTROLLER FOR OCDMA ENCODER SYSTEM

Jaafar, A.
Faculty of Electronic and Computer
Engineering
Universiti Teknikal Malaysia
Melaka (UTeM)
Hang Tuah Jaya, 76100 Durian
Tunggal, Melaka, Malaysia

Saffie, N.B.
Faculty of Electronic and Computer
Engineering
Universiti Teknikal Malaysia
Melaka (UTeM)
Hang Tuah Jaya, 76100 Durian
Tunggal, Melaka, Malaysia

M.H. Sulaiman
Faculty of Electronic and Computer
Engineering
Universiti Teknikal Malaysia
Melaka (UTeM)
Hang Tuah Jaya, 76100 Durian
Tunggal, Melaka, Malaysia

Abstract: This paper proposed a design of optical switching controller using FPGA for OCDMA encoder system. The encoder is one of the new technologies that use to transmit the coded data in the optical communication system by using FPGA and optical switches. It is providing a high security for data transmission due to all data will be transmitting in binary code form. The output signals from FPGA are coded with a binary code that given to an optical switch before it signal modulate with the carrier and transmit to the receiver. In this paper, AA and 55 data were used for source 1 and source 2. It is generated sample data and sent packet data to the FPGA and stored it into RAM. The simulation results have done by using software Verilog Spartan 2 programming to simulate. After that the output will produces at waveform to display the output. The main function of FPGA controlling unit is producing single pulse and configuring optical switching system.

Keywords: Field programmable gate array (FPGA), Code Division Multiple Access (CDMA), Optical Code Division Multiple Access (OCDMA), Linear Feedback Shift Register (LFSR), pseudo-noise (PN), Verilog

1. INTRODUCTION

Interest in OCDMA has been steadily growing during recent decades. That trend is accelerating due to fiber penetration in the first mile and the establishment of PON technology as a pragmatic solution for residential access. OCDMA is one promising technique for next-generation broadband access network with the following advantages: asynchronous access capability, accurate time of arrival measurements, and flexibility of user allocation, ability to support variable bit rate, busty traffic and security against unauthorized users. OCDMA is a very attractive multi-access technique that can be used for local area network (LAN) and the first one mile. Moreover, the OCDMA method is preferable for multiplexing in the optical domain because it uses broadband widths in optical devices for the electrical CDMA method and the electrical-to-optical (E/O) conversion. OCDMA is a multiplexing procedure by which each communication channel is distinguished by a specific optical code rather than a wavelength or time-slot [11]. An encoding operation optically transforms each data bit before transmission. At the receiver, the reverse decoding operation is required to recover the original data. OCDMA is the use of OCDMA technology to arbitrate channel access among multiple network nodes in a distributed fashion. There are many different kinds of OCDMA encoder/decoders use optical delay lines or optical switches with optical orthogonal code (OOC) for the time domain fiber Bragg grating (FBG) or AWGs and OOCs for the optical frequency domain, and FBGs or AWGs for optical wavelength-hopping / time spreading (TS) [4]. AWG-based encoder/decoder has the unique capability of simultaneously processing multiple time-spreading optical codes (OCs) with single device, which makes it a potential cost-effective device to be used in the central office of OCDMA network to reduce the number of encoder/decoders. The AWG-based encoder/decoder also has very high power contrast ratio

(PCR) (15~20 dB) between auto- and cross-correlation signals, which means the interference value could be significantly reduced (up to 20 dB) with the short OC [1-3].

Code-division multiple-access (CDMA) communication system allows multiple users to access the network simultaneously using unique codes. [9-10] Optical CDMA has the advantage of using optical processing to perform certain network applications, like addressing and routing without resorting to complicated multiplexers or demultiplexers. The asynchronous data transmission can simplify network management and control. OCDMA is an attractive candidate for LAN application. Normally, OCDMA can provide a secure network connection providing dynamic encoding. OCDMA (Optical CDMA) communication systems do not require any time or frequency management. It can operate asynchronously without centralized control and it does not suffer from packet collisions. As a result, OCDMA systems have lower latencies than TDMA or In a OCDMA system each bit is divided up into N time periods, called chips. By sending short optical pulse during some chip intervals, but no others, an optical signature sequence or codeword can be created. Each user on the OCDMA system has a unique signature sequence. The encoder of the each transmitter represents each 1bit by sending signature sequence, however a binary 0 bit is not encoded and is represented using all-zero sequence. Since each bit is represented by a pattern of lit and unlit chips, the bandwidth of the data stream is increased. The OCDMA is encoded data is then send to an 'N x N' known as star coupler (in local area network) or '1xN' coupler (in an access network) and broadcast to all nodes. The crosstalk between different users sharing the common fiber channel, known as MAI (Multiple Access Interface) is usually the dominant source of bit errors in an O-CDMA system. The main difference of OCDMA systems from wireless CDMA is the code structure.

Optical systems are mainly intensity modulated and hence the chips in the OCDMA system are alternating '1' s and '0' s instead of '-1' s and '+1' s. In OCDMA the overlap of optical pulses results in the addition of optical power. Optimum CDMA codes have been found assuming bipolar signals which can take on positive and negative values, though optical signal can also be processed coherently to provide bipolar signals. Recently practical optical fiber systems use direct detection and can therefore process only unipolar signals consisting of "1" s and "0" s. CDMA codes consisting entirely of '1' s and '0' s are referred to as optical codes and several variants have been recently proposed in many literature. An important class of CDMA optical codes is so called set of OOCs (Orthogonal Optical Codes)[5]. OOC is a family of (0,1) sequences with good auto and cross correlation properties. The (1,0) sequences of OOC are called its code words. In other words, the cross -correlation of two distinct CDMA codes must take a value as low as possible.

Field Programmable Gate Arrays (FPGAs) are programmable semiconductor devices that are based around a matrix of Configurable Logic Blocks (CLBs) connected through programmable interconnects. Verilog HDL is one of the two most common Hardware Description Language (HDL) used by integrated circuit (IC) designers. The other one is VHDL[6]. HDL's allows the design to be simulated earlier in the design cycle in order to correct errors or experiment with different architectures. Design describes in HDL are technology independent, easy to design and simulate and are usually more readable than schematics normally for the large circuits. Verilog can be used to describe designs at four levels of abstraction which is algorithms level (much like c code with if, case and loop statements). Register transfer level (RTL uses registers connected by Boolean equations). Gate level (interconnected AND, NOR etc). switch level (the switches are MOS transistors inside gates). The language also defines construct that can used to simulate the input and output. Mostly, Verilog is used as an input for synthesis programs and will generate a gate level description and analyze for the coding. Some Verilog construct are not synthesizable. The code is written will greatly affect the size and speed of the synthesizer. Normally, the readers want to synthesize their coding, so non synthesizable construct should be used only for test benches [12-14].

2. OVERVIEW SYSTEM

Figure 1 shows the operation of Code Division Multiple Access process. At the transmitter, two data sources generated digital data sequences which are individually multiplied using two orthogonal code sequences. Both of data user is identified by its unique code. The serial data sequences are multiplied by their corresponding PN sequences. The PN code sequence can be easily generated using Linear Feedback Shift Register (LFSR). The orthogonal code sequences are generated by periodically repeating orthogonal codes are at a rate much greater than the source data rate. The modulated sequence has wider frequency spectrum more than the original source sequence. It is called spread spectrum data sequence. The two spread spectrum data sequences are finally summed up and transmitted over a common channel.

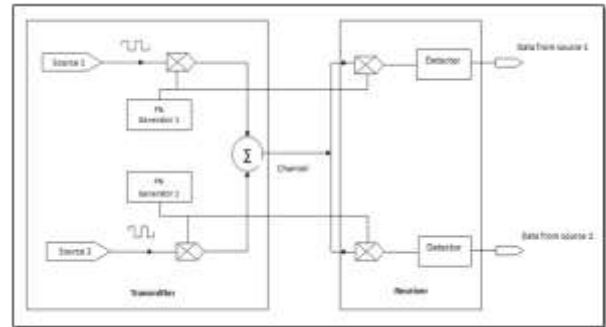


Figure 1: Block Diagram of Code Division Multiple Access

2.1 pseudo-noise(PN) Generator Operation

This operation consist 7-bit PN code generator by using three stages Linear Feedback Shift Register (LFSR). The logic circuit diagram of three stage LFSR implement in Verilog coding is shown in figure above. This operation of three stage of LFSR used D flip flop gate. PN generators are separated by two parts, which entities were implemented, one of each for two sources. The 3-bit initialize (seed) was set within the Verilog coding itself for each entity. The PN generator for source 1 is initialized with (S2 S1 S0) = 110. This input are generates PN code 1100101. For PN generator for source 2 is initialized with (S2 S1 S0) = 111. This input are generates PN code 1110010. The operation of PN generator by using three stages LFSR shows at figure 2 below. The PN generator components generate the respective PN sequences for two sources. To ensure that seven chips in the PN sequence align exactly with one bit of serial data, the PN sequence is generated at the master clock rate example master clock rate is assumed to be 7x. The serial data sequence is generated at one seven rate of master clock. This operation also used XOR gate.

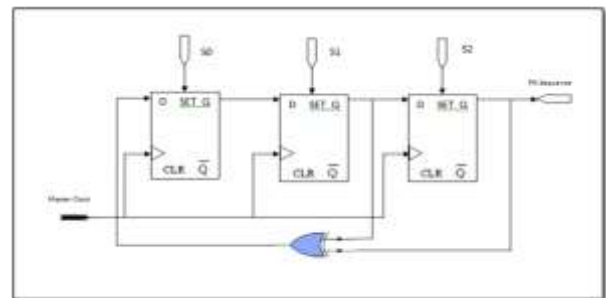


Figure 2: Three stage of LFSR

2.2 Linear Feedback Shift Register (LFSR)

The PN generator for spread spectrum is usually implemented as a circuit consisting of exclusive OR gates and a shift register, called a Linear Feedback Shift Register (LFSR)[7-8]. The LFSR is a string of 1-bit storage devices. Each device has an output line, which indicates the value currently stored, and an input line. At discrete time instants, known as clock times, the value in the storage device is replaced by the value indicated by its input line. The entire LFSR is clocked simultaneously, causing a 1-bit shift along the entire register.

2.3 Data Source

This component reads in 8-bit data from keyboard interface and shifts out the data serially. It is composed of two entities Divide by eight and an 8-bit Parallel In Serial Out (piso.vhd) This component is driven by clock of one seventh master

clock rate and the output bit changes every 7th master clock cycle. The serial output is synchronized with PN sequence such that one data bit period equals seven PN code chips.

2.4 Channel

Channel is the medium through which the signals are transmitted by using fiber optic cable [7]. A communication channel can be generally characterized as linear filters and signals transmitted over the channel suffer distortion due to channel response and noise. In CDMA, since all user channels operate simultaneously in the same RF band, the interference due to the multiple users in same RF channel become more important factor and it plays vital role in deciding the performance of the communication system. A mobile channel includes effects of multipath fading and noise. In the simulation however, only Additive White Gaussian Noise (AWGN) channel has been used, which is the simplest channel models, from analysis point of view. A built in command `awgn()` was used to model AWGN channel.

In the simulation communication link has been modeled as a forward channel where each user data is uniquely identified and spread using Walsh codes. As mentioned earlier, the perfect orthogonality of Walsh codes significantly reduces the probability of error at receiver. In order to simulate bit errors due to multipath effect, intercellular interferers, random non orthogonal data were added onto the AWGN channel. These interfering signals are not orthogonal with the Walsh codes used for the channels in the concerned cell and thus causes substantial amount of error. However in order to simulate error due to the multipath interferences from the users operating in the same cell or the interferences coming from users in other cells, random data was added in the channel that may not be exactly orthogonal to the Walsh codes. At PN generator operation use three stages Linear Feedback Shift Register (LFSR). Whereby use three gate XOR to shift the binary code.

3. EXPERIMENTAL RESULTS

At the PN Generator process, we need to use the three stages LFSR to generate the output data. Input 110 seed to PN Generator and will shift using three stages of LFSR used XOR gate. The output after process shows in table 1 below.

Input 110 = Output 1100101

Table 1. PN generator for input 110

Clk	Q2	Q1	Q0	Output Sequence
1	0	1	1	1
2	0	0	1	1
3	1	0	0	0
4	0	1	0	0
5	1	0	1	1
6	1	1	0	0
7	1	1	1	1
8	0	1	1	1
9	0	0	1	1
10	1	0	0	0
11	0	1	0	0
12	1	0	1	1

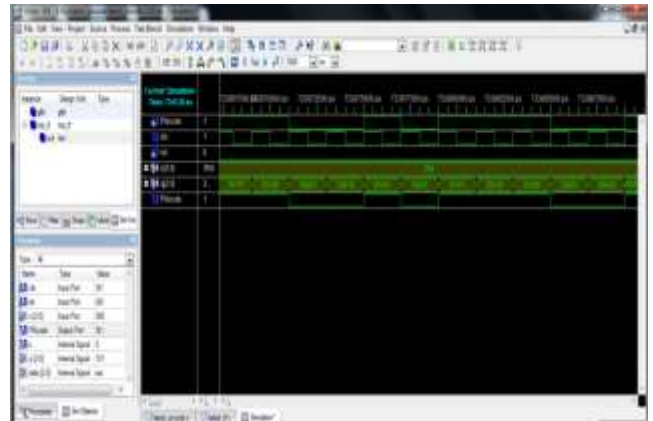


Figure 3: Simulation result for PN generator 110

At the PN Generator process, we need to use the three stages LFSR to generate the output data. Input 111 seed to PN Generator and will shift using three stages of LFSR used XOR gate. The output after process shows in table 2 below.

Input 111 = Output 1110010

Table 2. PN generator for input 111

Clk	Q2	Q1	Q0	Output Sequence
1	1	1	1	1
2	0	1	1	1
3	0	0	1	1
4	1	0	0	0
5	0	1	0	0
6	1	0	1	1
7	1	1	0	0
8	1	1	1	1
9	0	1	1	1
10	1	0	1	1
11	1	1	0	0
12	1	1	1	1

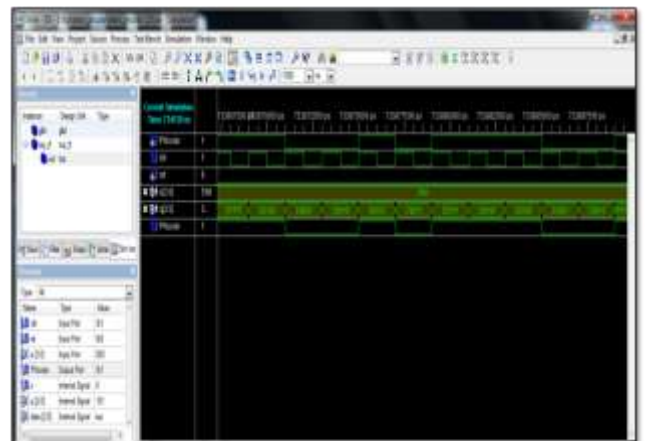


Figure 4: Simulation result for coding 111

The final output for transmitted data encoder can prove from calculation.

Input from data 1 was set as AA for encoder 0

$$\begin{aligned} \text{Encoder 0} &= \text{AA} + \text{PN code 110} \\ &= 10101010 + 1100101 \\ &= 10\text{F} \end{aligned} \quad [\text{Eqn 1}]$$

Input from data 2 was set as 55 for encoder 1

$$\begin{aligned} \text{Encoder 1} &= 55 + \text{PN code 111} \\ &= 1010101 + 1110010 \\ &= \text{C7} \end{aligned} \quad [\text{Eqn 2}]$$

Encoder final = Encoder 0 + Encoder 1

$$\begin{aligned} &= 10\text{F} + \text{C7} \\ &= 1\text{D6} \end{aligned} \quad [\text{Eqn 3}]$$

4. CONCLUSION

This paper was carried out two major objectives of implementing a CDMA system at simulating a CDMA communication system in Verilog. The first objective was successfully developed and for the second objective was successfully accomplished after extensive designing, coding and testing. A two users CDMA system was implemented in Verilog and synthesized onto an FPGA board. The operation of the system was successfully verified. The various PN Generator topologies were studied and they were synthesized using Xilinx ISE software. Device Utilization and No of Logic Blocks of each topology were noted down and compared with each other. The simulations have done by using Verilog code.

5. ACKNOWLEDGMENTS

This research is funded by the grant from Faculty of Electronic and Computer Engineering, Universiti Teknikal Malaysia Melaka (UTeM) with project number of PJP/2013/FKEKK(47B)/S01274.

6. REFERENCES

- [1] Harold P.E. Stern, Samy A. Mahmoud, "Theory of Code Division Multiplexing, Communication Systems: Analysis and Design", Prentice Hall PTR.
- [2] Y. Wang, et al., "Design and experiment of an all-optical label using FBG-based encoder/decoders," 2009, pp. 727811-1.
- [3] M. S. Ab-Rahman, et al., "Development of Low-cost OCDMA Encoder based on Arrayed Waveguide Gratings (AWGs) and Optical Switches," World Academy of Science, Engineering and Technology, vol. 46, 2008.
- [4] Shah, "Code Division Multiple Access : A Tutorial", p6-10, Wireless Communication, Rowan University, 1999.

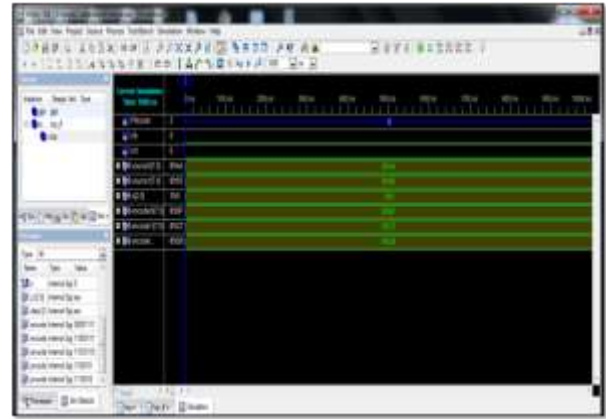


Figure 5: Simulation result for final encoder (Transmit)

Figure 5 above shows the simulation result for final encoder (transmitted) data using FPGA as a controller. The simulation result has shown at figure above. After running simulation complete, the result for encoder 0 is 10F and for encoder 1 is C7. For final encoder the data transmit is 1D6. The output is 8 bit and show in hex code. The value of 1 is carry flag.

- [5] C. Zhang, et al., "Experimental demonstration of tunable multiple optical orthogonal codes sequences-based optical label for optical packets switching," Optics Communications, vol. 283, pp. 932-938, 2010.
- [6] B. Zeidman and Z. Consulting, Introduction to verilog: IEEE Press, 2000.
- [7] K. Skahill, "VHDL for Programmable Logic", Addison-Wesley, 1999.
- [8] A. Dhital, "CDMA System: Simulation and Implementation," 2006.
- [9] S. Prakash, et al., "Compact field programmable gate array (FPGA) controller for aircraft/aerospace structures," 2008.
- [10] M. Akiyama, et al., "High-performance pulsed-power generator controlled by FPGA," Plasma Science, IEEE Transactions on, vol. 38, pp. 2588-2592, 2010.
- [11] M. Zainudin, H. Radi, and S. Abdullah, "Face Recognition using Principle Component Analysis (PCA) and Linear Discriminant Analysis (LDA)," ijens.org, no. 05, 2012.
- [12] A. Jaafar, N. Arasid, N. Hashim, A. Latiff, and H. Rafis, "Three Bit Subtraction Circuit via Field Programmable Gate Array," ijaret.org, vol. 1, no. Viii, pp. 1-13, 2013.
- [13] Jaafar, A., Hamidon A.H., A.A. Latiff, Hazli Rafis, H.H.M. Yusof, W.H.M. Saad, "Modelling of swarm communication," Int. J. Adv. Res. Electr. Electron. Instrum. Eng., vol. 2, no. 8, pp. 3725-3731, 2013
- [14] Latiff, A. A., et al. "Comparative Study on Single-And Double-Pass Configurations for Serial Dual-Stage High Concentration EDFA.", Int. J. of Research in Eng. and Tech., vol. 2, no.12, pp. 139-143, 2013.

Performance Analysis of Actual Step and Mesh Voltage of Substation Grounding System with the variation of Length and Number of Ground Rod

Shwe Myint
Electrical Power Engineering Department,
Mandalay Technological University,
Mandalay, Myanmar

Yan Aung Oo
Electrical Power Engineering Department,
Mandalay Technological University,
Mandalay, Myanmar

Abstract: The performance of Earthing grid system is very important to ensure the human and protective devices in safe environment. Actual Step and Mesh voltage of a substation must keep under the maximum allowable limits under fault condition. Ground potential rise, GPR is greatly influence on actual step and mesh voltage of substation grounding system. Ground potential rise also mainly depends on the length and numbers of ground rods and grid spacing. This paper presents performance analysis of actual step and mesh voltages of a substation grounding system under the variance of length and number of ground rods. The performance result is also carried out by using current injection method and with the help of MULTISIM simulation software.

Key words: Actual touch and step voltage, current injection method, earth rod, earthing grid design, grid resistance, Ground Potential Rise, MULTISIM simulation software.

1. INTRODUCTION

The main objectives of a substation grounding system is to provide a path that carry electric currents into the earth under normal and fault conditions without exceeding any operating and equipment limits or adversely affecting continuity of service and to assure that a person in the vicinity of grounded facilities is not exposed to the danger of critical electric shock. So, it is necessary to calculate the safety step and touch voltage level for the person who works in the vicinity of grounded facilities in normal condition. Under normal condition, i.e., the horizontal elements do not have any failures, the touch and step voltages, shown in figure 1, will not be dangerous for staff or equipment that stand on the top stratum of soil. But, during abnormal situations such as insulation failures of equipment, lightening strokes and etc., high currents flows through the grounding grid. In this situations a very high voltage levels of actual step and touch voltage will be introduced and the environment will not safe anymore. The highest values of voltage rise will be on the edge elements of the grounding device [4]. The value of actual mesh voltage and step voltage must less than tolerable touch and step voltage even under the fault condition. Therefore, it is also very important to design the earthing grid system so that the actual step and touch voltage level would be maintained within

the allowable limits. The actual step and touch voltage level mainly depend on the ground potential rise, GPR. The more the GPR rise, the higher the actual step and touch voltage level. The major parameters of the earthing grid design are soil resistivity, spacing and size of horizontal grid and length and number of vertical earth rods. The variance of length and number of vertical earth rods under the uniform soil resistivity will greatly affect the value of ground potential rise. The main purpose of this paper is to choose the most safety earthing grid design over the three following cases: a substation-

- (i) with 38x10 m ground rods earthing system,
- (ii) with 76x5m ground rods earthing system and
- (iii)with 126x3 m ground rods earthing system under the same uniform soil area.

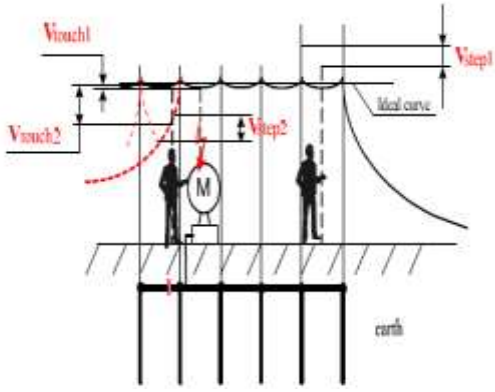


Figure 1: Touch and Step voltage Exposure

2. BUILDING EARTH GRID MODEL

Since grounding grid is mainly composed of horizontal earth electrodes and vertical earth rods, it is needed to make a circuit model that represents the horizontal and vertical element. All the horizontal and vertical elements shown in figure 2 represent not only self-resistance of conductors itself (steel, copper, copper clad etc.) but also lumped-resistances to earth of the buried in soil conductors. It consists of three parts: (i) a self-resistance of the conductor material, (ii) contact resistance between material of the element and soil and (iii) soil resistivity itself. Thus, the total resistance that resists to the current which leaks from the element to earth can be presented as:

$$R_{hor(ver)} = R_{me} + R_{cont} + R_{soil} \quad (1)$$

However, the first two elements (R_{me} and R_{cont}) have very small values and often can be neglected.

The resistance of the vertical and horizontal elements in the soil can be calculated as

$$R_{ver} = \frac{\rho_{ev}}{2\pi \cdot l_{ver}} \cdot \left(\ln \frac{2l_{ver}}{d_{ver}} + 0.5 \ln \frac{4l_{ver} + 7 \cdot t}{l_{ver} + 7 \cdot t} \right) \quad (2)$$

Where, $\rho_{e.v}$ – equivalent resistance of earth for the vertical elements, Ωm ; t – depth of the grounding grid; l_{ver} – length of the vertical element; d_{ver} – diameter of the vertical element

$$R_{hor} = \frac{\rho_{e.h}}{2\pi \cdot l_{hor}} \cdot \ln \frac{l_{hor}^2}{t \cdot d_{hor}} \quad (3)$$

Where, $\rho_{e.h}$ – equivalent resistance of the earth for the horizontal elements, Ωm ; l_{hor} – length of the horizontal element, d_{hor} – diameter of the horizontal element.

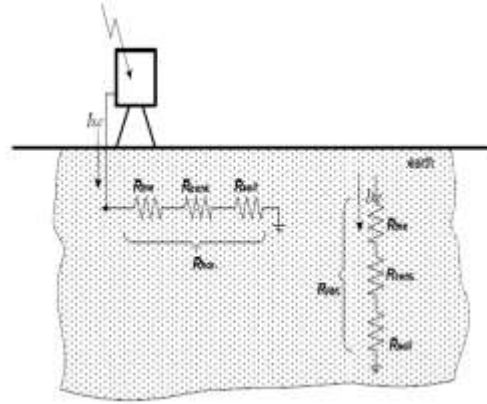


Figure 2: Equivalent scheme of the horizontal and vertical elements in the soil

The resistance of earth R_{soil} depends on the resistivity of different soil stratum (ρ_1, ρ_2, ρ_3 etc.). The number of layers (stratum) can differ from one area to another depending on the soil structure.

2.1. Sample data for test system

This test system is carried from [B-3] rectangular grid with ground rod in IEEE std-80. the detail design data can be seen from the following table.

Table 1: Sample data for substation

Fault duration, t_f	0.5s
Soil resistivity, ρ	400 Ωm
Crushed rock resistivity, ρ_s	2500 Ωm
Depth of grid burial, t	0.5 m
Available grounding area, A	64 m x 84 m
Grid spacing, D	7 m
Ground rod length	10 m for 38 rods
Allowable touch voltage	838.2 V
Diameter of ground rod	0.01 m
frequency	60Hz

By taking required data from table 1, the values of horizontal and vertical elements of the substation grounding grid can be calculated by using equation (2) and (3) in order to make a simulation model in MULTISIM.

2.2. Calculation of horizontal and vertical resistance

Case (1), is the base case and grid layout dimension is shown in figure 3. The area of the grid layout is 63m x 84m. In this case, there are 38 vertical earth rods, each of 10m long. The calculated values are, $R_{hor} = 90.45\Omega$ and $R_{ver} = 52.113\Omega$.

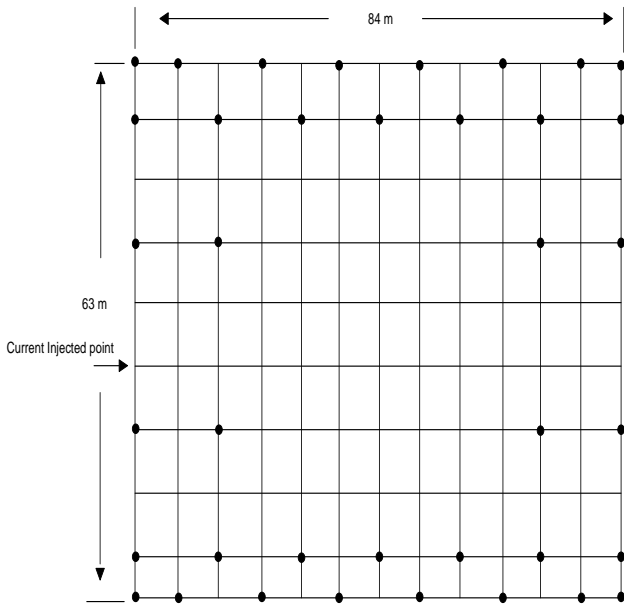


Figure 3: case (i) grid layout plan with 10 m x 38 rods

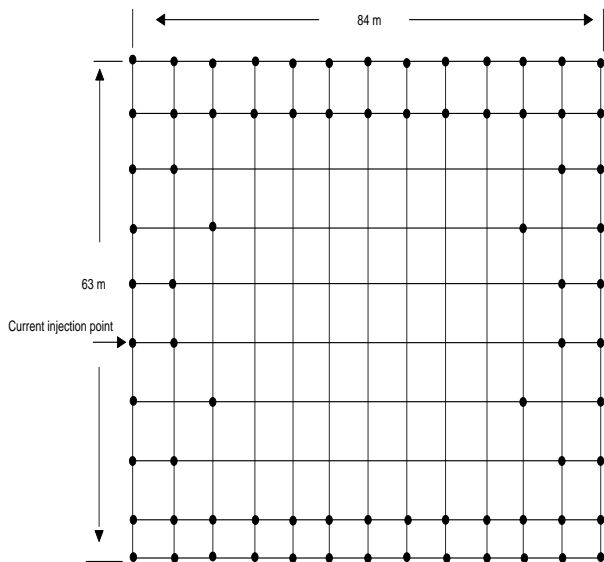


Figure 4: case (ii) grid layout plan with 5 m x 76 rods

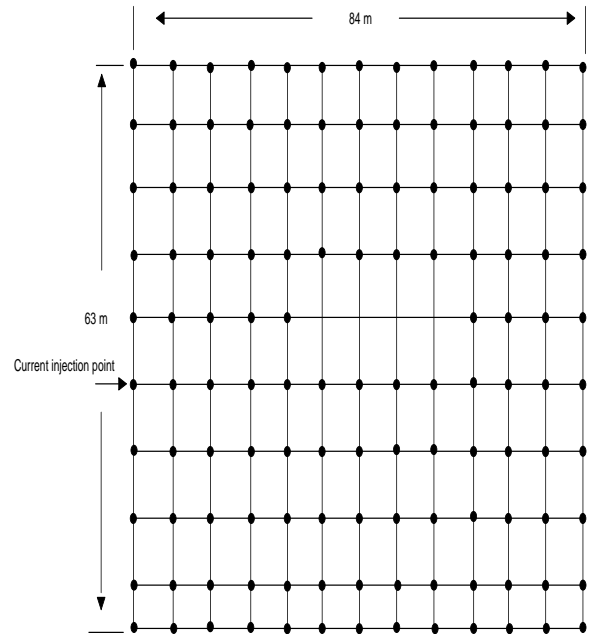


Figure 5: case (iii) grid layout plan with 3 m x 126 Rods

In case (ii), the value of ground rod length 10m is reduced to 5m while another 38 ground rods each of 5m long is added to the existing elements and keeping the other parameters remain the same. So, net total of 76 vertical ground rods is introduced. In this condition, only the value of vertical element is changed to $R_{ver} = 94.43\Omega$. Earthing grid layout design for case (ii) is shown in figure 4.

Also in case (iii), the length of vertical ground rod is reduced to 3m and the numbers of vertical earth rods are increased to total of 126, as shown in figure 5. Other parameter are taken as the previous cases. Here, the value of the vertical earth rod for case (iii), $R_{ver} = 144.968\Omega$.

3. CALCULATION OF EARTHING GRID RESISTANCE

A good grounding system provides a low resistance to remote earth in order to minimize the GPR. For most transmission and other large substations, the ground resistance is usually about 1Ω or less. In smaller distribution substations, the usually acceptable range is from 1Ω to 5Ω , depending on the local conditions.

Sverak [B132] expanded Equation to take into account the effect of grid depth;

$$R_g = \rho \left[\frac{1}{L_T} + \frac{1}{\sqrt{20A}} \left(1 + \frac{1}{1+h\sqrt{\frac{20}{A}}} \right) \right] \quad (5)$$

Where,

- R_g is the substation ground resistance in Ω
- ρ is the soil resistivity in $\Omega \cdot m$
- A is the area occupied by the ground grid in m^2
- h is the depth of the grid in m
- L_T is the total buried length of conductors in m

When the practical data are substituted in equation, the same value of earthing grid resistance have same at 2.62 Ω because case (i),(ii),(iii) have not changed total burial length of the grid and soil resistivity.

4. CALCULATION OF MAXIMUM STEP AND MESH VOLTAGES

4.1. Mesh voltage (E_m)

The mesh voltage values are obtained as a product of the geometrical factor, K_m ; a corrective factor, K_i , which accounts for some of the error introduced by the assumptions made in deriving K_m ; the soil resistivity, ρ ; and the average current per unit of effective buried length of the grounding system conductor (I_G/L_M)

$$E_m = \frac{\rho \cdot K_m \cdot K_i \cdot I_G}{L_M} \quad (6)$$

The geometrical factor K_m (Sverak [B132]), is as follows

$$K_m = \frac{1}{2\pi} \left[\ln \frac{D^2}{16 \cdot h \cdot d} + \frac{(D+2 \cdot h)^2}{8 \cdot D \cdot d} - \frac{h}{4 \cdot d} \right] + \frac{K_{ii}}{K_h} \cdot \ln \left[\frac{8}{\pi(2 \cdot n - 1)} \right] \quad (7)$$

For grids with ground rods along the perimeter, or for grids with ground rods in the grid corners, as well as both along the perimeter and throughout the grid area,

$$K_{ii} = 1 \quad (8)$$

For grids with no ground rods or grids with only a few ground rods, none located in the corners or on the perimeter.

$$K_{ii} = \frac{1}{(2 \cdot n)^{\frac{2}{n}}} \quad (9)$$

$$K_h = \sqrt{1 + \frac{h}{h_o}} \quad (10)$$

Where, h is actual grid depth

h_o is grid reference depth (1 m)

Using four grid shape components developed in Thapar, Gerez, Balakrishnan, and Blank [B144], the effective number of parallel conductors in a given grid, n , can be made applicable to rectangular or irregularly shaped grids that represent the number of parallel conductors of an equivalent rectangular grid.

$$n = n_a \cdot n_b \cdot n_c \cdot n_d \quad (11)$$

$$\text{Where, } n_a = \frac{2 \cdot L_c}{L_p} \quad (12)$$

$n_b = 1$ for square grids

$n_c = 1$ for square and rectangular grids

$n_d = 1$ for square, rectangular and l-shaped grids

Otherwise,

$$n_b = \sqrt{\frac{L_p}{4 \cdot \sqrt{A}}} \quad (13)$$

$$n_c = \left[\frac{L_x \cdot L_y}{A} \right]^{0.7 \cdot A} \quad (14)$$

$$n_d = \frac{D_m}{\sqrt{L_x^2 + L_y^2}} \quad (15)$$

Where, L_C is the total length of the conductor in the horizontal grid in m, L_p is the peripheral length of the grid in m, A is the area of the grid in m^2 , L_x is the maximum length of the grid in the x direction in m, L_y is the maximum length of the grid in the y direction in m, D_m is the maximum distance between any two points on the grid in m and D , h , and d are defined in Table 1.

The irregularity factor, K_i , used in conjunction with the above defined n is:

$$K_i = 0.6440.148 \cdot n \quad (16)$$

For grids with no ground rods, or grids with only a few ground rods scattered throughout the grid, but none located in the corners or along the perimeter of the grid, the effective buried length, L_M , is

$$L_M = L_C + L_R \quad (17)$$

Where, L_R is the total length of all ground rods in m

For grids with ground rods in the corners, as well as along the perimeter and throughout the grid, the effective buried length,

$$L_M = L_C + \left[1.55 + 1.22 \left(\frac{L_r}{\sqrt{L_x^2 + L_y^2}} \right) \right] L_R \quad (18)$$

Where, L_r is the length of each ground rod in m.

The mutual impedance among elements in the grid can be presented by multiplication factor "F" from [3];

$$F = 1 + \frac{\left(\frac{2 + \frac{N}{4}}{4} \right) \frac{l}{d_s}}{\ln \left(\frac{4l}{a} \right) - 1} \quad (19)$$

Where, N – the total number of rods in rod bed, d_s – the smallest distance between the adjacent rods, m, l – the length of each conductor, a – radius of the conductor.

This F factor increases the resistance of each element of the grid or finally the value of voltage on the grid. It happens because electromagnetic fields of all elements of the grid influence on each other due to the small distance between them as shown in figure 6. Thus, it artificially increases the value of resistance of each element.

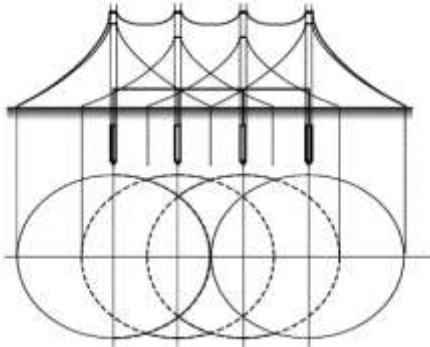


Figure 6: Influence of the element on each other [4].

4.2. Step voltage (E_s)

The step voltage values are obtained as a product of the geometrical factor, K_s ; the corrective factor, K_i ; the soil resistivity, ρ ; and the average current per unit of buried length of grounding system conductor (I_G/L_S).

$$E_s = \frac{\rho \cdot K_s \cdot K_i \cdot I_G}{L_s} \quad (20)$$

For grids with or without ground rods, the effective buried conductor length, L_s , is

$$L_s = 0.75 \cdot L_C + 0.85 \cdot L_R \quad (21)$$

The maximum step voltage is assumed to occur over a distance of 1 m, beginning at and extending outside of the perimeter conductor at the angle bisecting the most extreme corner of the grid. For the usual burial depth of $0.25 \text{ m} < h < 2.5 \text{ m}$ (Sverak [B132]), K_s is

$$K_s = \frac{1}{\pi} \left[\frac{1}{2 \cdot h} + \frac{1}{D+h} + \frac{1}{D} (1 - 0.5^{n-2}) \right] \quad (22)$$

4.3. Performance Analysis of E_m and E_s

The performance of actual touch and step voltage depend on the variation of the parameters such as grid depth (h), grid area (A), diameters and total length of the buried conductors, soil resistivity (ρ) and so on. For existing substation, enhancement of actual touch and step voltage can only be obtained by the variation of length and number of ground rods. After calculating the horizontal and vertical resistances of the grounding grids, the simulation is carried out by injecting the defined fault current level. From simulation result of the MULTISIM, ground potential rise (GPR) at the point of injection is taken as the product value of two parameters (i.e., $\rho \times I_g$) in the network and inserted it into the calculation of actual step and touch voltages equation. Table 2 shows measured GPR values for all cases under uniform soil of $400 \text{ } \Omega\text{m}$ resistivity and various injected current levels. The values of GPR for case (ii) are 41.21% less than that of case (i) and 14.06% less than case (iii) respectively for all current injected values. In normal condition, the allowable touch voltage for substation is 838.2V. But, during fault condition, the actual touch voltages for every case become over the allowable limit at a certain injected current level. The three injected current levels of case (i), (ii) and (iii) that make the actual touch voltages over the allowable limit are 9kA, 14kA and 12kA respectively.

Table (2): Ground potential rise (GPR) at injection point

Injected current (A)	Case (i) GPR (V)	Case(ii) GPR (V)	Case (iii) GPR (V)
1000	36.4kV	21.4kV	24.9kV
2000	72.7kV	42.8kV	49.8kV
3000	109kV	64.2kV	74.7kV
4000	145kV	85.6kV	99.6kV
5000	182kV	107kV	125kV
6000	218kV	128kV	149kV
7000	255kV	150kV	174kV
8000	291kV	171kV	199kV
9000	327kV	193kV	224kV
10000	364kV	214kV	249kV
11000	400kV	235kV	274kV
12000	436kV	257kV	299kV
13000	473kV	278kV	324kV
14000	509kV	300kV	349kV
15000	546kV	321kV	374kV

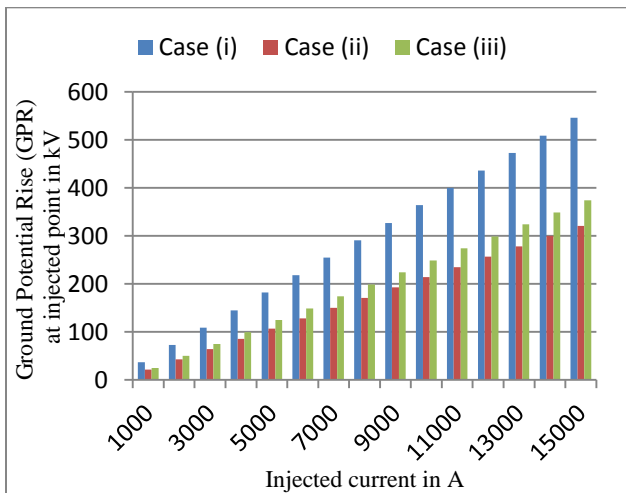


Figure 7: Variation of ground potential rise according to earthing grid design

The actual mesh and step voltages can be calculated by using equation (4) and (16) for this power plant. The mutual impedance among elements in the grid can be presented by multiplication factor “F” from [3]. In [2] multiplication of $\rho \times I_g$ is voltage at the node of the grid. So by using the values from Table (2). So, these calculated results are as follows:

Table (3) Actual mesh voltage at current injection point of the substation earthing grid

Injected current (A)	Case (i) Mesh Voltage (V)	Case (ii) Mesh Voltage (V)	Case (iii) Mesh Voltage (V)
1000	99.408	59.877	72.310
2000	198.544	119.754	144.619
3000	297.679	179.632	216.929
4000	395.995	239.509	289.238
5000	497.042	299.386	363
6000	595.358	358.144	432.696
7000	696.405	419.700	505.296
8000	794.721	478.458	577.896
9000	893.073	540.014	650.496
10000	994.084	598.772	723.096
11000	1092.400	657.530	795.696
12000	1190.716	719.086	868.296
13000	1291.763	777.844	940.896
14000	1390.079	839.400	1013.496
15000	1491.126	898.158	1086.096

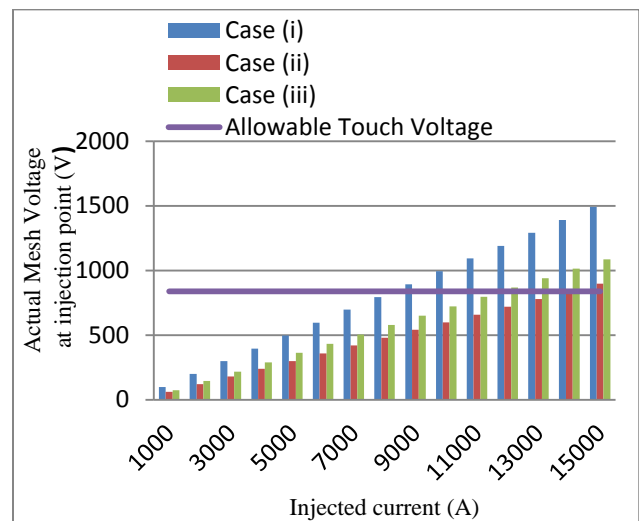


Figure 8: Actual Mesh Voltage performance of three earthing grid designs for a power plant

According to figure 8, the actual mesh voltage of case(ii) is within allowable touch potential up to 13000 A of injection, but case (iii) can safe up to 11000 A and case(i) can only safe to 8000A.

Table (4): Actual Step Voltage at current injection point of sample earthing grid for a substation

Injected current (A)	Case (i) Step Voltage (V)	Case (ii) Step Voltage (V)	Case (iii) Step Voltage (V)
1000	76.658	45.710	54.979
2000	153.106	91.421	109.958
3000	229.554	137.131	164.938
4000	305.370	182.842	219.917
5000	383.292	228.552	276.000
6000	459.108	273.408	328.992
7000	537.030	320.400	384.192
8000	612.846	365.256	439.392
9000	688.662	412.248	494.592
10000	766.584	457.104	549.792
11000	842.400	501.960	604.992
12000	918.216	548.952	660.192
13000	996.138	593.808	715.392
14000	1071.954	640.800	770.592
15000	1149.876	685.656	825.792

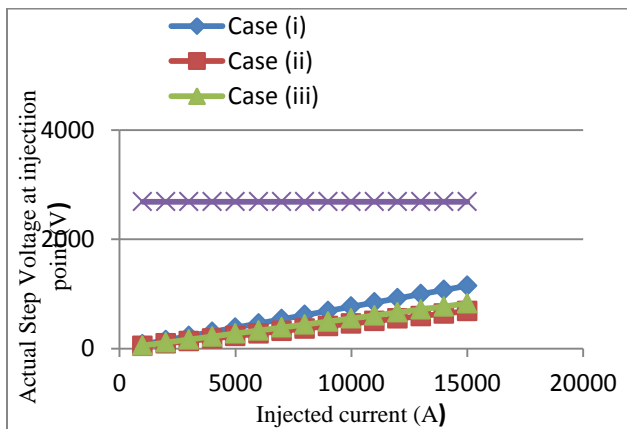


Figure 9: Actual step Voltage Variation at the injection point for three earthing grid design of a substation

5. CONCLUSIONS

This paper has presented performance analysis of actual step and mesh voltage of substation grounding system with the variation of length and number of vertical earth rod. The study involved a simulation with MULTISIM to an IEEE test system for three

different cases. It should be noted that earth grid resistance for three cases are equal because diameter of vertical earth rod and total burial length of the grid for all cases have not changed and it is under uniform soil resistivity. The values of GPR for case (ii) is 41.21% less than GPR of case (i). Moreover, case (ii) GPR is also 14.06% less than GPR of case (iii) for all current injected values. This shows that providing the more branches to flow the fault currents (i.e., adding more vertical earth rods) means the less potential rise in step and mesh voltage and GPR except for the case that the vertical earth rods resistance is greater than the horizontal elements resistance. In case (i), 9kA of injected fault current level makes the system actual touch voltage over the allowable limit while it is 12kA in case (iii). Since 14kA of injected fault current level can only make the system actual touch voltage over the allowable limit in case (ii), it can be seen that case (ii) only can withstand the highest injected current level among three cases. Thus case (ii) is the safest design among three alternatives. This paper covers only for the single layer of soil or uniform soil resistivity. For two layer soil model or non-uniform soil, the calculation of touch and step voltage performance should be considered the sign and value of reflection factor coefficient “k” according to upper layer and lower layer resistivity and also the depth of the top layer, ‘h’.

6. ACKNOWLEDGMENTS

The author would like to express grateful thanks to her supervisor Dr. Yan Aung Oo, Associate Professor and to all her teachers from Department of Electrical Power Engineering, Mandalay Technological University for their encouragement and helpful suggestions. And the author also would like to express her gratitude to her parents for their support and encouragement.

7. REFERENCE

- [1] IEEE Std.80-2000:”IEEE Guide for Safety in AC Substation Grounding”. The Institute of Electrical and Electronic Engineers, New York, 2000.
- [2] Li, Z., Chen, W., Fan, J., Lu, J. “A Novel Mathematical Modeling of Grounding System Buried in Multilayer Earth”. IEEE Transactions on Power Delivery, v. 21(3), 2006.

- [3] El Sherbiny M., "Simple Formulas for Calculating the Grounding Resistance of Rodbed Buried in Non-Uniform Soil". Proceedings of the 37th Midwest Symposium on Circuits and Systems University of Waterloo, Waterloo, Ontario, Canada N2L 3G1, 1954, pp. 1281-1284.
- [4] Yury Chikarov., "Safety Parameters of Grounding Devices at an Electric Power Plant". Department of Electrical and Electronic Engineering, Auckland University of Technology, Auckland, New Zealand.

Energy Efficient Three Phase Squirrel Cage Induction Motor fed AC Drives

D. Edison Selvaraj

Panimalar Engineering College
Chennai, India

C. Ruban Karthik

Mepco Schlenk Engg. College
Sivakasi, India

R. Arun

Mepco Schlenk Engg. College
Sivakasi, India

S. Geethadevi

Aurora Scientific and
Technological Institute
Uppal, Hyderabad, India

J. Ganesan

Sree Sowdambika College of
Engineering
Aruppukottai, India

Abstract: Three phase squirrel cage induction motors consume 60% of industrial electricity. 1% increase in efficiency of all the motors in India will save 500 MW powers which needs the initial generation cost of 2000 crores. The efficiency of an induction motor can be substantially improved by controlling the voltage to frequency ratio (V/Hz). Another method of improving the efficiency of induction motor was coating enameled copper wire filled with Al_2O_3 nano filler. One such method used in this project was carried out under serious literature survey. Based on the previous project works, actions were taken to use the enamel filled with nano filler as the coating for the induction motor to improve its efficiency. Definitely, there will be a tremendous improvement in the efficiency of the induction motor and hence the motor can be called as "High Efficiency Squirrel Cage Induction Motor".

Keywords: Induction motor, Enamel, Nano fillers, Load test, Efficiency

1. INTRODUCTION

Induction motors were widely used in fans, centrifugal pumps, blowers, lifts, cranes, hoists and so on. The efficiency of the induction motor depends upon the insulation used [1-3]. For motors, the enamel was used for three purposes: impregnation, coating and adhesion. The efficiency of the induction motor can be increased by adding the nano fillers with the enamel which was used as coating for the windings of the motor [3-6]. In this paper, the efficiency of the normal three phase squirrel cage induction motor and the Al_2O_3 nano filled enamel coated three phase squirrel cage induction motor was analyzed and the results were compared with each other.

2. PREPARATION AND CHARACTERIZATION OF Al_2O_3 NANO FILLER

The micro powders of Al_2O_3 were crushed into nano powders by Ball Mill method. The SEM images of Al_2O_3 before and after Ball Mill show the particle size of the powders. The particle size was augmented by SEM images [7-9]. These SEM results show that the prepared particles of Al_2O_3 were in the nm range.

2.1 SEM analysis before Synthesis

The particle size of Al_2O_3 before ball mill method was shown in Figure 1.

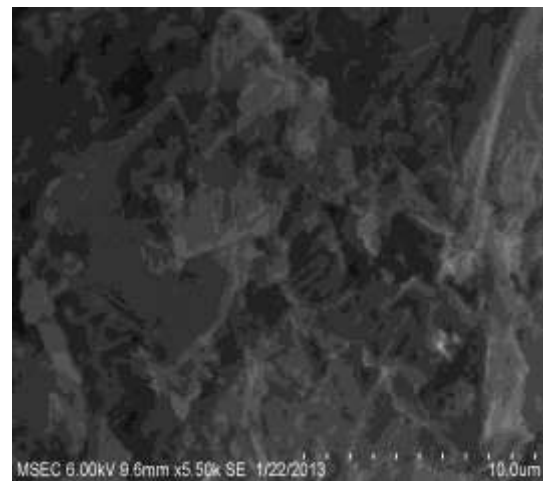


Figure 1 SEM analysis of Al_2O_3 at 10 μm

2.2 SEM analysis After Synthesis

From the analyzed SEM image the particles were in the form of nano metric range varies for one area to other. The sizes of the particles as shown in figure 2 were in the range from 40 to 100 nm size.

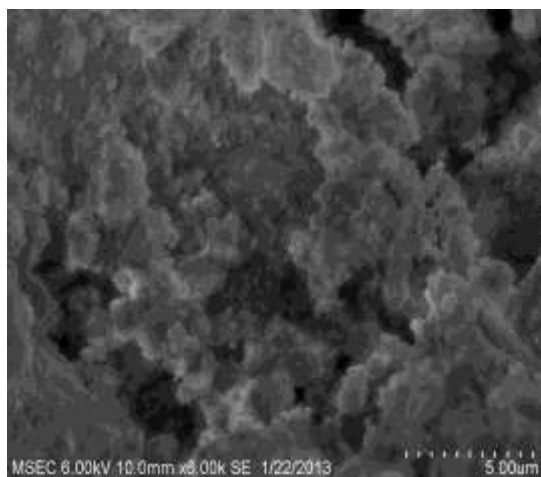


Figure 2 SEM analysis of Al₂O₃ at 5 μm

3. COATING OF THE AL₂O₃ NANO FILLED ENAMEL TO THE WINDINGS OF THE MOTOR

The nano powder of Al₂O₃ were taken and mixed with the enamel by using ultrasonic vibrator [9-12]. Further, this enamel was coated on the windings of the three phase squirrel cage induction motor. The Figure 5 shows the Al₂O₃ Nano filled enamel coated Induction motor.



Figure 5 Al₂O₃Nanocomposite filled enamel coated Induction motor

The specifications of the three phase squirrel cage induction motor were shown below in the Table 1.

Table 1 Specifications of the three phase squirrel cage induction motor

Quantity	Rating
Power	1.5 HP
Speed	1450 rpm
Current	3.45 A
Voltage	415

4. EXPERIMENTAL ANALYSIS

4.1 Performance Analysis of Squirrel Cage Induction Motor – Circle diagram Method

This analysis was done by doing open and short circuit test. By calculating the open and short circuit current and voltage the losses were found using circle diagram method. From the circle diagram it was found that the losses were reduced in nano coated motor. It was shown in the table 2 and 3.

Table 2 Open circuit and short circuit test readings for ordinary induction motor

Open Circuit Test	Voc	Ioc	Woc
	415	1.3	80
Short Circuit Test	Vsc	Isc	Wsc
	95	3.45	210

Table 3 Open circuit and short circuit test readings for Nanocoated induction motor

Open Circuit Test	Voc	Ioc	Woc
	415	1.3	65
Short Circuit Test	Vsc	Isc	Wsc
	95	3.45	180



Figure 6 Snap shot of open and short circuit test

Efficiency was analyzed by conducting load test in ordinary as well stator enameled with nano composite motor [11-13]. The results obtained were successful for nano coated motor. The efficiency of nano coated motor increased to 4 percent. This is mainly due to reduction of dielectric losses in nano coated motor. The readings were calculated for various slip values and shown in Table 4. Figure 7 shows the Efficiency comparison of various motors.

Table 4 Efficiency comparison for ordinary and nano coated motor

Slip	Efficiency of normal induction motor in %	Efficiency of nano coated induction motor in %
0.02	74.95	79.07
0.04	71.5	76.32
0.06	67.50	72.73
0.08	63	67.3
0.1	59.85	63.8

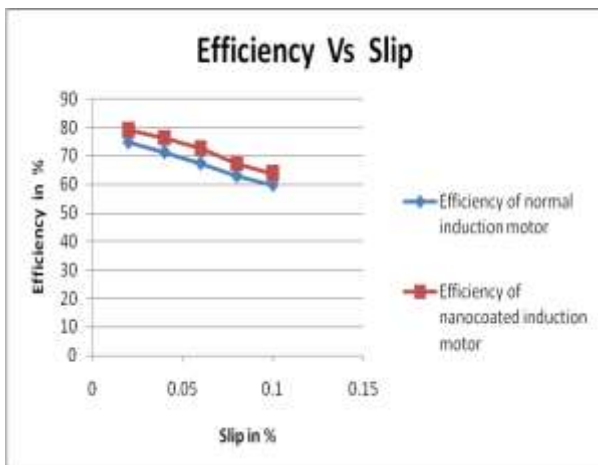


Figure 7 Efficiency comparison of various motors

4.2 Performance Analysis of Squirrel Cage Induction Motor – Direct loading Method

The load test was conducted on the ordinary induction motor and the nano coated induction motor. The performance of the motor were obtained for induction motor by this method. The output power, current, efficiency, powerfactor and speed of the motor were measured during this testing. The maximum efficiency obtained from an ordinary induction motor was 75%. The maximum efficiency obtained from nano coated induction motor was 79%. The efficiency of the motor was increased due to the reduction in harmonic and dielectric losses.

5. CONCLUSION

The efficiency of the induction motor was increased by 4% by adding Al₂O₃ nano filler to the enamel used as the coating for the windings of the three phase squirrel cage induction motor. Hence, the overall performance of the induction motor was also increased by adding Al₂O₃ nano filler to the enamel used in the induction motor. The speed fluctuations were also less and smooth when compared to that of the ordinary induction motor.

6. ACKNOWLEDGEMENT

Thank God and His almighty power to finish His research work by using me, my project guide and my parents for His ultimate work.

7. REFERENCES

- [1] Selvaraj, D. Edison, et al. "Analysis of Efficiency, Thermal Withstanding Capacity and Electromagnetic Interference of Three Phase Squirrel Cage Induction Motor Coated with SiO₂ & TiO₂ nano composite Filled Enamel." International Journal of Science and Engineering Applications 1.1 (2012): 17-21.
- [2] Edison Selvaraj, D., C. Pugazhendhi Sugumaran, and A. Sivaprakash. "Characterization Of Electrical and Thermal Properties of Enamel Filled with Carbon Nanotubes." Proceedings of the Third International Conference on Trends in Information, Telecommunication and Computing. Springer New York, 2013.
- [3] Selvaraj, D. Edison. "Partial discharge characteristics of enamel filled with micro and nano composite of siO₂ and TiO₂." International Journal of Science and Engineering Applications 1.2 (2012): 95-101.
- [4] Selvaraj, D. Edison. "Characterization of dielectric properties of the enamel filled with carbon nano tubes for the frequency range of 50 Hz-5 MHz" International Journal of Science and Engineering Applications 1.2 (2012): 102-106.
- [5] Selvaraj, D. Edison, and C. Pugazhendhi Sugumaran. "Comparative Analysis of Dielectric Properties of Enamel Filled with Various Nano fillers such as ZrO₂, Al₂O₃, CNT and ZnO." International Journal of Science and Engineering Applications 1.1 (2012): 51-55.
- [6] Babu, B. Gurukarthik, D. Edison Selvaraj, R. Srinivas, B. Guru Prakash, and R. Vishnu. "Analysis of Relative Permittivity and Tan Delta Characteristics of Silicone Rubber Based Nano-composites." International Journal of Scientific Engineering and Technology, pp.2201-206, 2012.
- [7] D.EdisonSelvaraj,J.Ganesan. "Experimental Analysis of Efficiency and Thermal Withstanding Capacity of Three Phase Squirrel Cage Induction Motor Coated with SiO₂ & TiO₂ Nano Composite Filled Enamel", International Journal of Engineering Sciences, Vol (2), No (4), 2013. pp. 115-118.

- [8] Lieutenant Ganesan. J, Jeyadevi.S.Dr, and Edison Selvaraj. D, "Performance Analysis of Single Phase Induction Motor Coated with Al_2O_3 Nano Filler Mixed Enamel" ACEEE International Journal on Recent Trends in Engineering & Technology Vol. 10, No. 1, Jan 2014.
- [9] Edison Selvaraj. D, Pugazhendhi Sugumaran. C, Lieutenant Ganesan. J, Ramathilagam. J, "Analysis of Dielectric and Thermal Properties of Polyamide Enamel Filled with Carbon Nano tubes" International Journal of Nano science, Vol.12, Issue 3, June 2013.
- [10] Lieutenant Ganesan. J, Edison Selvaraj. D, and Ramathilagam. J, "Experimental analysis of Thermal conductivity of enamel filled with micro and nano composite of SiO_2 and TiO_2 " International journal of Advanced Research in Electrical, Electronics and Instrumentation Engineering, Vol.2, Issue 7, pp. 2907-2912, 2013.
- [11] Lieutenant Ganesan. J, Jeyadevi. S. Dr, and Edison Selvaraj. D, "Reduction of Electromagnetic Interference in Single Phase Induction Motor by coating the winding with Al_2O_3 nano filler mixed Enamel" International journal of Advanced Research in Electrical, Electronics and Instrumentation Engineering, Vol.2, Issue7, pp. 2913-2916, 2013.
- [12] Lieutenant Ganesan. J, Edison Selvaraj. D, and Selva Kumar. B, "High Efficiency Induction Motor", International journal of Advanced Research in Electrical, Electronics and Instrumentation Engineering, Vol.2, Issue 2, pp. 750-754, 2013.
- [13] Lieutenant Ganesan. J, and Edison Selvaraj. D, "Analysis of Thermal and Electrical Properties of Enamel Filled with Various Nano fillers such as ZrO_2 , Al_2O_3 and CNT", International Journal of Engineering Research, Vol.2, Issue 2, pp. 182-186, 2013.

Comparative Study on Dynamic Analysis of Irregular Building with Shear Walls

Le Yee Mon
Civil Engineering Department,
Mandalay Technological University,
Mandalay, Myanmar

Abstract: South East Asia including Myanmar is situated in secondary seismic belt. Therefore, it is necessary to pay special attention of the effect of earthquake in designing the high-rise building. Shear walls are very common in high rise reinforced concrete building. In this study, comparative analysis of high-rise reinforced concrete irregular building with shear walls are present. The frame type of proposed building is used the special RC moment resisting frame. It belongs to seismic zone 4. This is why, seismic forces are essentially considered in the analysis of this building and shear walls are also provided to resist seismic forces. Structural members are designed according to ACI Code 318-02. The structure is analysed by using ETABS v 9.7.1 software. Load consideration is based on UBC-97. All necessary load combinations are considered in shear walls analysis and frame analysis. In addition wind load, seismic load is considered as external lateral load in the dynamic analysis. In dynamic analysis; Response Spectrum method is used. In this project, study of 14 storey building is presented with some investigation which is analyzed by changing various location of shear wall for determining parameters like storey drift, storey shear and storey moment .

Key words: Shear wall; Response Spectrum method; ETABS software; dynamic comparisons

1. INTRODUCTION

Myanmar is a developing country and the population of Myanmar is increasing more and more. Mandalay, the second largest city of Myanmar, lies in a serious earthquake more and more. Therefore, in constructing the residential buildings, it should be designed to resist not only gravity loading such as dead load and live load but also horizontal loading such as wind load and seismic load. The proposed building being located in Mandalay should be designed to withstand not only gravity forces but also lateral forces, as Mandalay is situated in flat terrain and severe earthquake zone. Structural wall system is much stiffer than a frame system and its performance during an earthquake is better than the performance of the frame system. In this study, shear walls are provided for reinforced concrete building to obtain the required stiffness and strength to withstand lateral load like wind and seismic. There are three types of shear wall. They are planar shear wall, coupled shear wall and core shear wall. To obtain the required stiffness and strength to withstand lateral load in high- rise building, shear walls are normally included some frames of the building. They are continuous down to the base to which they are rigidly attached to form vertical cantilever. Therefore, the magnitudes of moment and horizontal shear are found to be maximized at the base and they become less as they become high. The positions of shear walls within a building are dictated by functional requirements. They may or may not suit structural planning. Building sites, architectural interests may lead, on the other hand, to positions of walls that one undesirable from a structural point of view. Hence, structural designers will often be in the position desirable locations for shear wall in order to optimize lateral force resistance. Shear wall are efficient, both in terms of construction cost and effectiveness in minimizing

earthquake damage in structural and non- structural. Shear walls can reduce total deflection and the beams connected to the shear wall need to have the larger member size.

2. PREPARATION

2.1 Site Location and Structural System

The type of building is fourteen storey Y- shaped reinforced concrete residential building with shear walls. The location of proposed building is in Mandalay (seismic zone 4) and only the wind velocity of 80 mph is considered. The maximum dimension is 128 ft in Global- X direction and 136 ft in Global-Y direction. The overall height of the structure is 159 ft. The type of occupancy is residential (four unit for one storey). Model (1) is the special moment resisting frame (SMRF) structural system and other three models are composed of shear walls and SMRF (dual type) structural system. In this structure, response spectrum dynamic analysis is used. Plan and 3D view of proposed building are described in Figure 1, 2 and 3.

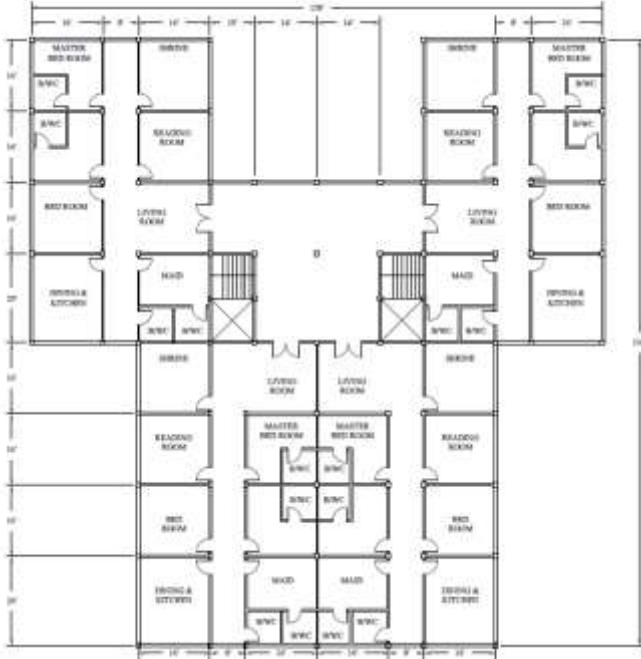


Figure 1: Plan of the proposed building

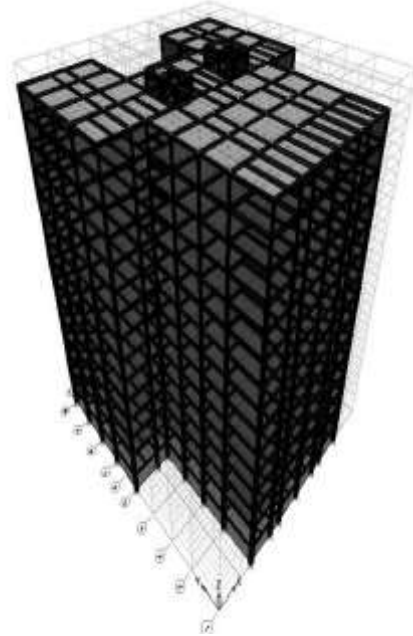


Figure 3: Three dimensional of the proposed building

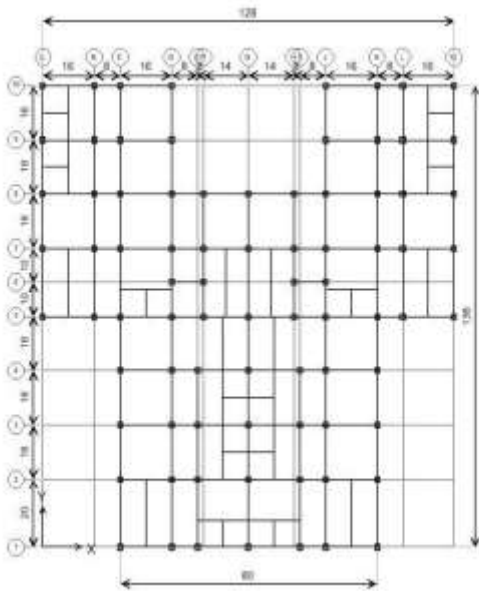


Figure 2: Plan of the proposed building

2.2 Material Properties

The strength of a structure depends on the strength of the materials from which it is made for this purpose; material strength is specified in standardized ways as a step to proceed the design of a structure.

Analysis property data

Weight per unit volume of concrete	150 lb/ft ³
Modulus of elasticity, E_c	3.122×10^6 lb/in ²
Poisson's ratio, μ	0.2
Coefficient of thermal expansion	5.5×10^{-6} in / in per °F

Design property data

Bending reinforcement yield stress (f_y)	50,000 lb/in ²
Shear reinforcement yield stress (f_y)	50,000 lb/in ²
Concrete cylinder strength (f_c)	3,000 lb/in ²

2.3 Loading considerations

The gravity loads considered in this design are dead load and live load. The lateral loads of wind load and earthquake load are calculated according to UBC-97.

(1) Gravity load

Dead load is defined as the results from the structure and all other permanently attached materials. They have constant magnitude and fixed location throughout the lifetime of the

structure. The characteristic feature of dead load is that they are permanent. Live loads are produced by the use and occupancy of the building or other structure and do not include dead load, construction load and environmental loads. Live loads may be either fully or partially in place or not present at all and may also change a position.

Dead Load data are as follow:

Unit weight of concrete	150 lb/ft ³
4½" thick wall weight	50 lb/ft ²
9" thick wall weight	100 lb/ft ²
Superimposed dead load	20 psf
Weight of elevator	3 tons

Live Load data are as follow:

Live load on residential area	40 lb/ft ²
Live load on roof	30 lb/ft ²
Live load on stair case	100lb/ft ²
Weight of water	249.6 psf

(2)Wind Load

Every building or structure and every portion shall be designed and constructed to resist the wind effects. Wind shall be assumed to come from any horizontal direction.

Wind load data are as follow:

Exposure type	Type B
Basic wind velocity	80 mph
Important factor	1
Windward coefficient	0.8
Leeward coefficient	0.5
Method used	Normal force method

(3)Earthquake Load

Earthquake load data are as follow;

Location	Mandalay
Seismic zone	Zone 4
Zone factor, Z	0.4
Soil type	S _D
Importance factor, I	1.0
Response modification factor, R	8.5
Seismic coefficient, C _a	0.44 N _a
Seismic coefficient, C _v	0.64 N _v
Near source factor, N _a	1.0
Near source factor, N _v	1.0
Analysis types	Dynamic Analysis

(4). Load Combinations

Design codes applied are ACI 318-02 and UBC-97. There are 30 numbers of load combinations which are used in the structural analysis.

NO	COMBINATIONS
COMB 1	1.4 D.L
COMB 2	1.2 D.L + 1.6L.L
COMB 3	1.2 D.L + L.L + 1.6 WXP
COMB 4	1.2 D.L + L.L - 1.6 WXP
COMB 5	1.2 D.L + L.L + 1.6 WXN
COMB 6	1.2 D.L + L.L - 1.6 WXN
COMB 7	1.2 D.L + L.L + 1.6 WYP
COMB 8	1.2 D.L + L.L - 1.6 WYP
COMB 9	1.2 D.L + L.L + 1.6 WYN
COMB 10	1.2 D.L + L.L - 1.6 WYN
COMB 11	1.2 D.L + 0.8 WXP
COMB 12	1.2 D.L - 0.8 WXP
COMB 13	1.2 D.L + 0.8 WXN
COMB 14	1.2 D.L - 0.8 WXN
COMB 15	1.2 D.L + 0.8 WYP
COMB 16	1.2 D.L - 0.8 WYP
COMB 17	1.2 D.L + 0.8 WYN
COMB 18	1.2 D.L - 0.8 WYN
COMB 19	0.9 D.L + 1.6 WXP
COMB 20	0.9 D.L - 1.6 WXP
COMB 21	0.9 D.L + 1.6 WXN
COMB 22	0.9 D.L - 1.6 WXN
COMB 23	0.9 D.L + 1.6 WYP
COMB 24	0.9 D.L - 1.6 WYP
COMB 25	0.9 D.L + 1.6 WYN
COMB 26	0.9 D.L - 1.6 WYN
COMB 27	1.4 D.L + L.L + SPECX
COMB 28	1.4 D.L + L.L + SPECY
COMB 29	0.9 D.L + SPECX
COMB 30	0.9 D.L + SPECY

3. METHODS OF DYNAMIC ANALYSIS

Dynamic analysis method

UBC-97 presents two types of dynamic analysis method for seismic response of a structure. They are;

- (1) Response spectrum analysis; and
- (2) Time-history analysis.

Of these two methods, response spectrum analysis is more convenient than time history analysis.

Response spectrum analysis

A response spectrum is the graphic representation of maximum response i.e. displacements, velocity and acceleration of a

damped single-degree-of-freedom system to a specified ground motion, plotted against the frequency or modal periods.

The response spectrum has the following characteristics.

(i) The model must be constructed as an elastic system i.e. the model must be moved and swayed by the excitation but there was no yielding.

(ii) A single value of damping is used for each model response.

In the response spectrum analysis, the distribution of seismic lateral force on the building is based on the deformed shapes of natural modes of vibration, which are determined from the distribution of mass and stiffness of the structure. From the response spectrum, a specified spectra value can be read. This value is used to calculate the theoretical maximum seismic force acting on a structure .

$$V = \frac{WS_a}{g}$$

where,

V=theoretical maximum seismic force

S_a=spectral acceleration read from spectrum

g=acceleration due to gravity (9.81 m/sec²)

W=effective weight

This analysis produces the complete time history response of joint displacements and member forces eliminating the time variable from the solution. For design purpose, the response spectrum should be representative of all seismic properties of specific site. If not, it may be constructed according to the spectral shape presented by UBC-97 by using site dependent seismic response coefficients.

Response spectrum analysis provides a rational and practical approximate method based on fundamental principles of dynamics and random vibration. Response spectrum analysis procedure involves the evaluation of the maximum value of structure response such as displacements and member forces for each mode of vibration using a spectrum of earthquake records. In response spectrum analysis model modes are first calculated, and then approximate total structural response is obtained by combining the model response in a statistical manner. Modal combination methods are Complete Quadratic Combination (CQC), Square Root of the Sum of the Square (SRSS), Absolute Sum Square (ABS), and General Modal Combination (GMC). In Complete Quadratic Combination (CQC), modal combination technique takes into account the statistical coupling between closely spaced modes caused by modal damping. Increasing the modal damping increases the coupling between closely spaced modes. Square Root of the Sum of the Square (SRSS) technique does not take into account any coupling of modes as do the CQC and GMC methods. In this study, CQC is used for modal combination. It is important to note that most building codes require the mode shapes to generate at least 90% of the participating mass of the structure in each of the three lateral directions.

Design Criteria for Dynamic Analysis

The procedure and limitations for the design of structures by UBC-97 are determined considering zoning, site characteristics, occupancy, configuration, structural system and height. For large or complex structures, static method of seismic analysis is

often deemed to be not accurate enough and many authorities demand dynamic analysis for certain type and size of structure. The dynamic lateral-force procedures are always acceptable for design when a structure has any of the conditions listed below.

- (1) Regular structure more than 240 ft in height and located in seismic zone 2, 3 and 4.
- (2) In seismic zone 2, 3 and 4, a structure with stiffness, weight, or geometric vertical irregularity and have more than five stories or 65 feet in height must be designed with dynamic analysis.
- (3) Structure in seismic zone 3 and 4 having more than five stories or 65 ft with mixed vertical structural system.
- (4) In zone 2, 3 and 4 all structure having a period of greater than 0.7 second and located on soil profile type S_F [97 UBC].

Design Spectrum for Proposed Building

Design spectrum is a graph of time with respect to the peak ground acceleration. Design spectrum for proposed building is shown in Figure.4. The control periods T_s and T_o can be calculated by the formula;

$$C_a = 0.44, C_v = 0.64$$

$$C_t = 0.03, H = 159 \text{ ft}$$

$$T_s = \frac{C_v}{2.5 C_a} = 0.582, T_o = 0.2 T_s = 0.116,$$

$$T = C_t H^{3/4} = 1.34 \text{ sec}$$

When T = 0, spectral acceleration = C_a = 0.44

When T = T_o to T_s, spectral acceleration = 2.5C_a = 1.1

When T > T_s, spectral acceleration = C_v/T

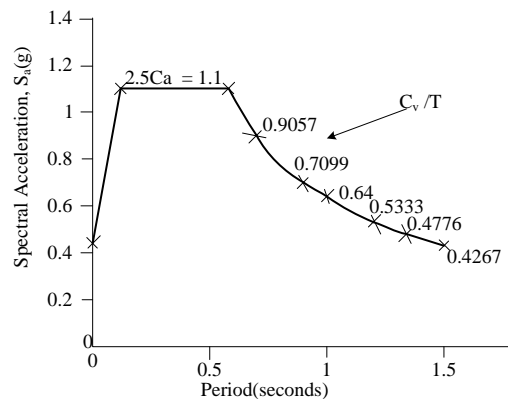


Figure 4: Design Spectrum for Proposed Building (5% damping)

4. STRUCTURAL MODELLING

Four buildings of 14 stories irregular in plan are modeled as of fixed base building and analyzed with soft computing tool ETABS V 9.7.1. Dynamic responses of building are studied. Four irregular model consists of symmetry in X direction of plan as well as elevation and Y direction plan asymmetry but elevation symmetric. In this study, the models are constructed with different contributions shear wall are used. The cross sectional dimensions of beams, columns and slabs are the same in the four models. And also, the material properties, loading and other data for wind and seismic forces are the same in the four models. The four cases of the building separately for comparison of storey drift, storey shear and storey moment are Case no. 1 .Without shear wall (Model 1), Case no. 2. When core shear wall placed at stair case & lift of building (Model 2), Case no.3. When core shear wall placed at stair case & lift of the building and planar shear walls placed at outer edge symmetrically parallel to X direction and planar shear walls placed at re-entrant corners (model 3). Case no. 4. When core shear wall placed at stair case & lift of building and planar shear walls placed at outer corner symmetrically X and Y direction (Model 4). Model 1,2,3,4 are shown in figure 5,6,7,8 respectively. The structural member sizes used in proposed both models are shown in the followings.

Column sizes	12"×12", 14"×14", 16"×16", 18"×18", 19"×19", 20"×20", 22"×22", 24"×24" and 26"×26"
Beam sizes	-10"×12", 10"×14", 10"×16", 10"×18", 12"×16", 12"×18", 14"×18", 14"×20"
Floor slab thickness	4.5"
Landing slab thickness	4.5"
Stair slab thickness	4.5"
Shear wall Thickness	14"
-GF to 2 nd floor	
-3 st floor to 7 th floor	12"
-8 th floor to Roof floor	10"

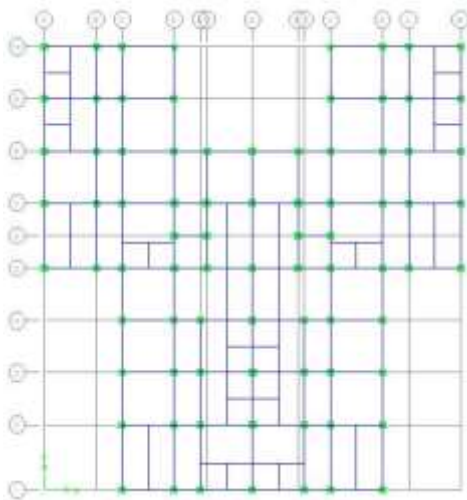


Figure 5: Plan of the non shear wall proposed building Model (1)

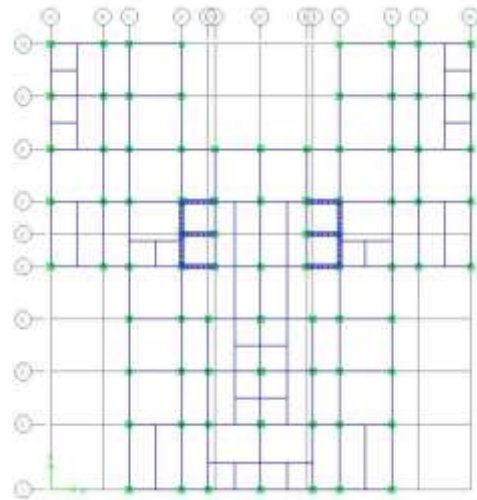


Figure 6: Plan of the core shear wall proposed building

Model (2)

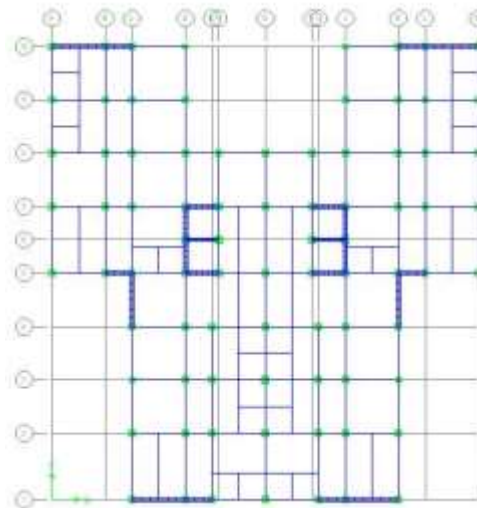


Figure7: Plan of the core and planar shear wall proposed building Model (3)

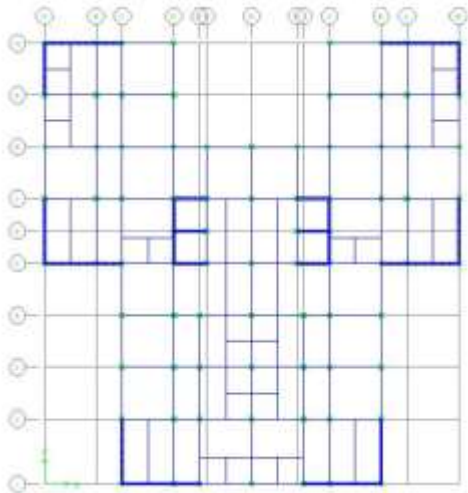


Figure8: Plan of the core and planar shear wall proposed building

Model (4)

Table 2. Storey Drifts in Y Direction Comparison

Story	Storey Drifts in Y Direction			
	Model 1	Model 2	Model 3	Model4
Roof	0.001031	0.001138	0.001095	0.000953
13	0.00123	0.001162	0.001115	0.000953
12	0.001291	0.001173	0.001126	0.000957
11	0.001409	0.001179	0.001131	0.000959
10	0.001503	0.00118	0.001129	0.000951
9	0.001563	0.00117	0.001118	0.000934
8	0.001603	0.001144	0.001092	0.000904
7	0.001604	0.001091	0.001039	0.000853
6	0.001552	0.001028	0.00098	0.000798
5	0.001525	0.000957	0.000908	0.000732
4	0.001539	0.000867	0.000818	0.000651
3	0.001637	0.000759	0.00071	0.000555
2	0.00163	0.00062	0.000571	0.000438
1	0.001812	0.000485	0.000425	0.000313
GF	0.001087	0.000264	0.000224	0.000162

5. ANALYSIS RESULT

The analysis of all the frame models that includes different location of shear walls has been done by using software ETABS and the results are shown below. The parameters which are to be studied are storey drift, storey shear and storey moment. Results obtained from the analysis are recorded for the four cases of the building separately for comparison of storey drift, storey shear and storey moment.

Table 1. Storey Drifts in X Direction Comparison

Story	Storey Drifts in X Direction			
	Model 1	Model 2	Model 3	Model4
Roof	0.001058	0.001426	0.00125	0.001044
13	0.001287	0.001505	0.001263	0.001056
12	0.001398	0.001547	0.001268	0.001061
11	0.001464	0.001592	0.001268	0.00106
10	0.001631	0.001648	0.001259	0.001052
9	0.00167	0.001656	0.001236	0.001031
8	0.001741	0.00167	0.001196	0.000995
7	0.001704	0.001619	0.001134	0.000937
6	0.001678	0.001574	0.001059	0.000874
5	0.00163	0.00149	0.000969	0.000798
4	0.001627	0.001393	0.00086	0.000707
3	0.001608	0.001236	0.000731	0.000601
2	0.001704	0.001049	0.000573	0.00047
1	0.001815	0.00081	0.000389	0.000323
GF	0.00099	0.000403	0.000183	0.000172

Table 3. Storey Shears in X Direction Comparison

Story	Storey Shears in X Direction(Kips)			
	Model 1	Model2	Model 3	Model 4
RF	163.53	232.45	314.89	364.95
13	311.39	410.46	584.13	710.87
12	426	535.47	784.11	987.85
11	515.73	629.87	937.65	1213.35
10	587.66	708.43	1064.01	1402.75
9	646.08	777.11	1174.93	1566.39
8	696.5	840.61	1278.06	1712.68
7	742.93	904.28	1379.79	1850.84
6	789.9	970.95	1482.84	1984.76
5	840.75	1038.79	1584.37	2110.78
4	895.93	1106.5	1682.55	2226.86
3	952.75	1170.84	1771.4	2326.95
2	1006.88	1226.97	1844.68	2406.89
1	1051.43	1268.84	1897.57	2464.62
GF	1058.81	1276.39	1908.4	2478.39

Table 4. Storey Shears in Y Direction Comparison

Story	Storey Shears in Y Direction (Kips)			
	Model 1	Model2	Model 3	Model 4
RF	165.3	277.08	310.9	361.97
13	318.63	508.59	581.5	703.23
12	437.74	681.69	785.29	973.71
11	530.79	813.53	942.92	1191.83
10	606.63	920.43	1071.5	1374.08
9	668.08	1012.94	1183.04	1531.69
8	719.71	1098.43	1286.45	1673.36
7	767.51	1182.71	1387.84	1808.12
6	816.04	1269.38	1490.15	1939.88
5	867.58	1357.2	1591.93	2065.12
4	923.65	1445.01	1692.18	2182.01
3	982.64	1527.7	1784.59	2284.4
2	1039.55	1599.37	1863.37	2367.72
1	1086.53	1655.09	1924.75	2429.47
GF	1094.39	1666.12	1939.65	2445.55

Table 6. Storey Moment in Y Direction Comparison

Story	Storey Moment in Y Direction(Kips-in)			
	Model 1	Model2	Model 3	Model 4
RF	20405.83	29714.49	40077.82	46263.28
13	57562.01	78677.48	109873.9	131284.5
12	108005	141926.8	203014.8	249044.5
11	168475.7	215027.4	313111.5	392730.7
10	236619.2	295505.5	436049.4	557307.8
9	310480.9	381979.1	569398.4	739134
8	388736.8	473735.2	711928.8	935746.1
7	470612.8	570606.7	863275.8	1145788
6	555851.4	672882.2	1023590	1368550
5	644724.9	781046.2	1193143	1603430
4	737801.6	895524.1	1372134	1849826
3	835722.8	1016530	1560415	2106790
2	938951	1143965	1757373	2373040
1	1069698	1304438	2003398	2702395
GF	1182752	1442550	2213823	2982045

Table 5. Storey Moment in X Direction Comparison

Story	Storey Moment in X Direction(Kips-in)			
	Model 1	Model2	Model 3	Model 4
RF	20613.14	35305.51	39515.12	45848.44
13	58704.17	96109.32	109002.8	129958.5
12	110754.1	177193.8	202299	245999.8
11	173213.1	272903.2	313117.9	387005.7
10	243695.6	379458.5	437211.9	547914.8
9	320260.9	494553.6	571902.6	725179.6
8	401436.4	616997	715795.1	916493
7	486339.6	746400.5	868430.6	1120660
6	574692.6	882943	1029879	1337132
5	666725.8	1027055	1200391	1565475
4	762959.4	1179178	1380251	1805264
3	864064.2	1339512	1569467	2055739
2	970591.9	1507856	1767604	2315785
1	1105548	1719271	2015651	2638217
GF	1222281	1900833	2228254	2912511

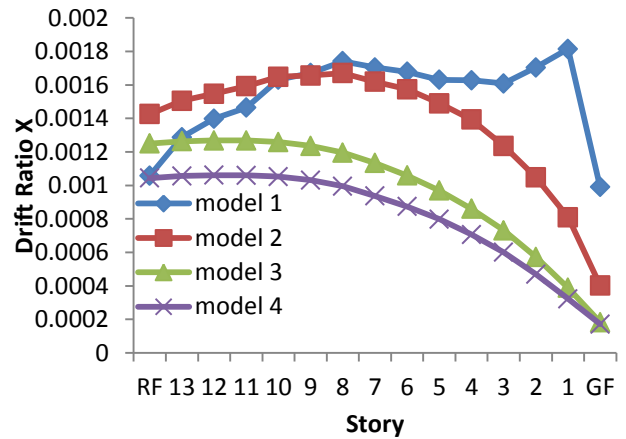


Figure.9 Comparison of Story Drift in X-direction

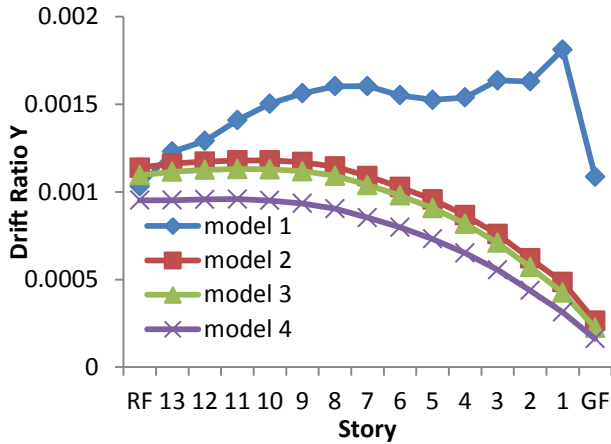


Figure 10. Comparison of Story Drift in Y-direction

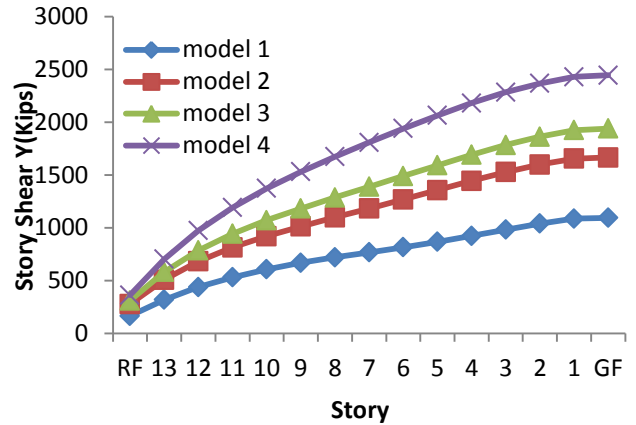


Figure 12. Comparison of Story Shear in Y-direction

The comparative study of storey drift values in X and Y directions for three models are represented in Table 1, Table 2 and Figure 9, Figure 10. The storey drift values of the non-shear wall structure (Model 1) is 2.24 times higher than that of Model (2) , 4.66 times greater than those of Model (3) and 5.62 times greater than those of Model (4) in X-direction at story 1. The storey drift values of the non-shear wall structure (Model 1) is 3.73 times higher than that of Model (2) , 4.26 times greater than those of Model (3) and 5.79 times greater than those of Model (4) in Y-direction at story 1. Thus, the story drift in structure with core shear wall and planar shear wall (Model 4) has the smallest value in both directions for all models.

The comparative study of storey shear values in X and Y directions for three models are represented in Table 3, Table 4 and Figure 11, Figure 12. In comparison of story shear in both directions, shears are increased steadily and maximum story shears are found in ground floor. The weight of the structure with core shear wall and planar shear wall (Model 4) is greater than other three structures .The storey shear values of the non-shear structure (Model 1) is 1.21times less than that of Model (2), 1.80 times less than those of Model (3) and 2.34 times less than those of Model (4) in X -direction at ground floor. Structure without shear wall has the least story shear and structure with core shear wall and planar shear wall (Model 4) has the greatest story shear.

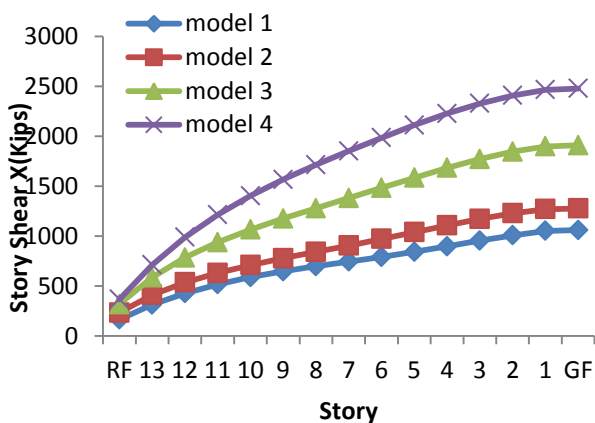


Figure 11. Comparison of Story Shear in X-direction

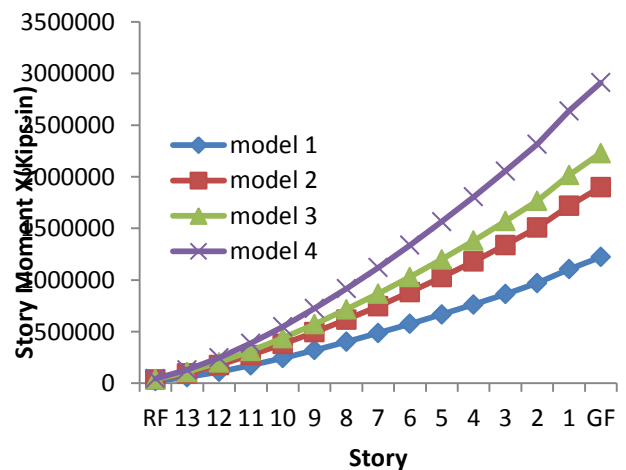


Figure 13. Comparison of Story Moment in X-direction

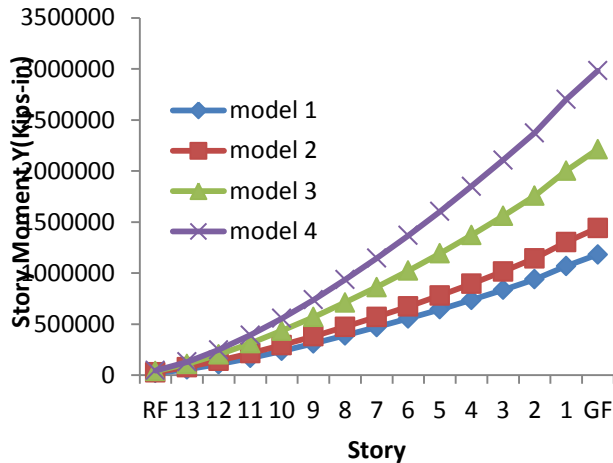


Figure 14. Comparison of Story Moment in Y-direction

The comparative study of storey moment values in X and Y directions for three models are represented in Table 5, Table 6 and Figure 13, Figure 14. In comparison of story moment in both directions, moments are increased steadily and maximum story moments are found in ground floor. The story moment is depending on the seismic load. So, the story moment is the largest at base. The storey moment values of the non-shear wall structure (Model 1) is 1.56 times slightly less than that of core shear wall structure and 1.82 times less than those of that of Model (3), and 2.38 times less than those of Model (4) in X-direction at ground floor. The storey moment values of the non-shear wall structure (Model 1) is 1.22 times slightly less than that of core shear wall structure and 1.87 times less than those of that of Model (3), and 2.52 times less than those of Model (4) in Y-direction at ground floor. Structure without shear wall has the least story moment and structure with core shear wall and planar shear wall (Model 4) has the greatest story moment.

4. DISCUSSIONS AND CONCLUSIONS

In this study, the analysis of fourteen storeyed Y-shaped high-rise reinforced concrete building in seismic zone 4 is done by ETABS v 9.7.1 software using response spectrum analysis. After analyzing the model, the stability checking is made for each model. Storey drift and torsional irregularity effect are checked by using UBC – 97 Formula. And then it is checked for overturning and resistance to sliding. The structural elements are designed by using American Concrete Institute (ACI 318-02). Shear wall are provided for lateral stability of reinforced concrete structure. The proposed building and the location of shear walls may or may not suit the functional requirements or the architectural interest. From the results of storey drift, storey drifts in X and Y-direction of model 4 are less than that of other three models. From the results of storey shears, storey shears in X and Y-direction of model 4 are greater than that of model 1, 2, 3. Storey shears are greatest at the base and gradually decrease from base to top storey for four models. Storey moments are slightly increased from top to bottom storey for all models. From comparative study, especially, model 4 is more reduced the

storey drift in both directions and it is suitable from structural point of view.

From the dynamic analysis of 14 storey RC building with plan irregularity we have got the following conclusions.

- (1) The influence of shear wall location on the selected irregular building is more stable by providing the location of shear walls in the symmetric side.
- (2) Story drift is increased as height of building increased and reduced at top floor so that shear wall frame interaction systems are very effective in resisting lateral forces induced by earthquake.
- (3) The selection of especially the location and amount of shear walls is of the highest importance in strengthening. Strengthening shear wall may vary in various positions according to their positions in the plan.

From the above study can conclude that model (4) shows better performance among the other models.

5. ACKNOWLEDGEMENT

The author wishes to extend grateful thanks to her supervisor, Dr. San Yu Khaing, Associate Professor, Department of Civil Engineering, Mandalay Technological University, for her supervision, critical reading of manuscript, and tolerance helped in all the time of this research work. The author specially thanks to all her teachers from Department of Civil Engineering, Mandalay Technological University and her family for their supports and encouragement and also thanks to all her friends.

6. REFERENCES

- [10Nyi] Nyi Hla Nge, U.: *Reinforced Concrete Design*, 1st Ed., Pioneer Group, Yangon, (2010).
- [01Lin] Lindeburg, M. R, and Baradar, M.: *Seismic Design of Building Structures: A Professional's Introduction to Earthquake Forces and Design Details*, 8th Ed., Professional Publications, Inc, (2001).
- [02Ano] Anonymous: *Building Code Requirements for Structural Concrete (ACI 318-02) and Commentary (ACI 318R-02)*, USA: American Concrete Institute (2002).
- [97Nil] Nilson, A. H.: *Design of Concrete Structure*, 12th Ed., McGraw-Hill, Inc.(1997).
- [97UBC] Uniform Building Code.: *Structural Engineering Design Provisions, Volume 2*, 8th International Conference of Building Officials, (1997).
- [91Smi] Smith, B. S, and Coull, A.: *Tall Building Structure: Analysis And Design*", John Wiley and Sons, Inc (1991).

Pulse Compression Method for Radar Signal Processing

Thin Thin Mar

Department of Electronic Engineering
Mandalay Technological University
Mandalay, Myanmar

Su Su Yi Mon

Department of Electronic Engineering
Mandalay Technological University
Mandalay, Myanmar

Abstract: One fundamental issue in designing a good radar system is its capability to resolve two small targets that are located at long range with very small separation between them. Pulse compression techniques are used in radar systems to avail the benefits of large range detection capability of long duration pulse and high range resolution capability of short duration pulse. In these techniques a long duration pulse is used which is frequency modulated before transmission and the received signal is passed through a match filter to accumulate the energy into a short pulse. A matched filter is used for pulse compression to achieve high signal-to-noise ratio (SNR). Two important factors to be considered for radar waveform design are range resolution and maximum range detection. Range resolution is the ability of the radar to separate closely spaced targets and it is related to the pulse width of the waveform. The narrower the pulse width the better is the range resolution. But, if the pulse width is decreased, the amount of energy in the pulse is decreased and hence maximum range detection gets reduced. To overcome this problem pulse compression techniques are used in the radar systems. In this paper, the pulse compression technique is described to resolve two small targets that are located at long range with very small separation between them.

Keywords: Pulse compression, Radar, LFM, Matched filter, Range Resolution

1. INTRODUCTION

The rapid advances in digital technology made many theoretical capabilities practical with digital signal processing and digital data processing. Radar signal processing is defined as the manipulation of the received signal, represented in digital format, to extract the desired information whilst rejecting unwanted signals. Pulse compression allowed the use of long waveforms to obtain high energy simultaneously achieves the resolution of a short pulse by internal modulation of the long pulse. The resolution is the ability of radar to distinguish targets that are closely spaced together in either range or bearing. The internal modulation may be binary phase coding, polyphase coding, frequency modulation, and frequency stepping. There are many advantages of using pulse compression techniques in the radar field. They include reduction of peak power, relevant reduction of high voltages in radar transmitter, protection against detection by radar detectors, significant improvement of range resolution, relevant reduction in clutter troubles and protection against jamming coming from spread spectrum action [1].

Pulse compression employs a modulated "long" pulse to achieve the range resolution of a "short" pulse without the need for high peak transmit power. Short pulses are better for range resolution, but contradict with energy, long range detection, carrier frequency and SNR. Long pulses are better for signal reception, but contradict with range resolution and minimum range. At the transmitter, the signal has relatively small amplitude for ease to generate and is large in time to ensure enough energy in the signal. At the receiver, the signal has very high amplitude to be detected and is small in time.

In pulse compression technique, the transmitted signal is frequency or phase modulated and the received signal is processed using a specific filter called "matched filter". A matched filter is a linear network that maximizes the output peak-signal to noise ratio of a radar receiver which in turn maximizes the detect ability of a target. There are several methods of pulse compression that have been used in the past. The most popular of them is linear

frequency modulation (LFM) which was invented by R.H. Dickie in 1945 [1]. The other pulse compression techniques are Binary phase codes, Polyphase codes, Barker codes, Costas codes, Nonlinear Frequency Modulation etc. In this paper, we developed MATLAB code to study the LFM pulse compression technique with chirp diversity.

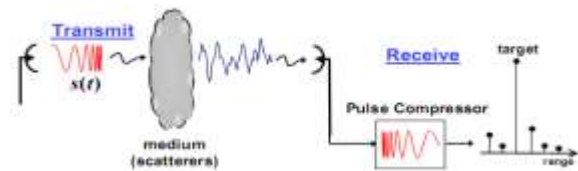


Figure 1. Pulse Compression

2. PULSE COMPRESSION ALGORITHM

The maximum detection range depends upon the strength of the received echo. To get high strength reflected echo the transmitted pulse should have more energy for long distance transmission since it gets attenuated during the course of transmission. The energy content in the pulse is proportional to the duration as well as the peak power of the pulse. The product of peak power and duration of the pulse gives an estimate of the energy of the signal. A low peak power pulse with long duration provides the same energy as achieved in case of high peak power and short duration pulse. Shorter duration pulses achieve better range resolution. The range resolution r_{res} is expressed [2] as

$$r_{res} = \frac{c}{2B} \quad (1)$$

where B is the bandwidth of the pulse.

For unmodulated pulse, the time duration is inversely proportional to the bandwidth. If the bandwidth is high, then the duration of the pulse is short and hence this offers a superior range resolution. Practically, the pulse duration cannot be reduced indefinitely. According to Fourier theory a signal with bandwidth B cannot have duration shorter than

1/B i.e. its time-bandwidth (TB) product cannot be less than unity. A very short pulse requires high peak power to get adequate energy for large distance transmission. However, to handle high peak power the radar equipment become heavier, bigger and hence cost of this system increases. Therefore peak power of the pulse is always limited by the transmitter. A pulse having low peak power and longer duration is required at the transmitter for long range detection. At the output of the receiver, the pulse should have short width and high peak power to get better range resolution. Figure 2 illustrates two pulses having same energy with different pulse width and peak power. To get the advantages of larger range detection ability of long pulse and better range resolution ability of short pulse, pulse compression techniques are used in radar systems [2].

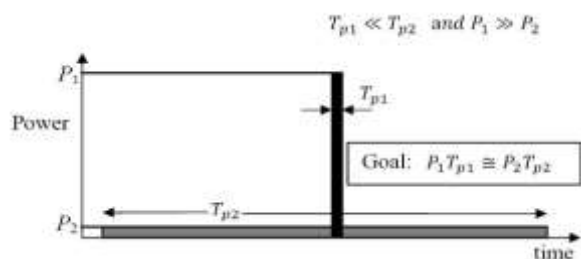


Figure 2. Transmitter and receiver ultimate signals

The range resolution depends on the bandwidth of a pulse but not necessarily on the duration of the pulse [3]. Some modulation techniques such as frequency and phase modulation are used to increase the bandwidth of a long duration pulse to get high range resolution having limited peak power. In pulse compression technique a pulse having long duration and low peak power is modulated either in frequency or phase before transmission and the received signal is passed through a filter to accumulate the energy in a short pulse. The pulse compression ratio (PCR) is defined as

$$PCR = \frac{\text{width of the pulse before compression}}{\text{width of the pulse after compression}} \quad (2)$$

2.1 LFM Algorithm

Linear frequency modulated (LFM) signals are used in most of the radar systems to achieve wide operating bandwidth. In this case the frequency increases (up chirp) or decreases (down chirp) linearly across the pulse. The instantaneous phase of the chirp signal is expressed as

$$\varphi(t) = 2\pi \left(f_0 t + \frac{1}{2} k t^2 \right) \quad (3)$$

where f_0 is the carrier frequency and k is the frequency sweep rate related to pulse duration T_p and bandwidth B as

$$k = \frac{B}{T_p} \quad (4)$$

The instantaneous frequency is given by

$$f(t) = \frac{d}{dt} \left(f_0 t + \frac{1}{2} k t^2 \right) = f_0 + kt \quad (5)$$

Equation (5) states that the instantaneous frequency is a linear function of time, and hence is called as linear frequency modulation. Figure 2 (a) shows the modulated sinusoidal signal that is transmitted by the pulse-compression radar. The pulse is characterized by its pulse width, which in the case of a pulse-compression radar is called the uncompressed pulse

width, T . This pulse width is one of the critical characteristics of the pulse-compression radar.

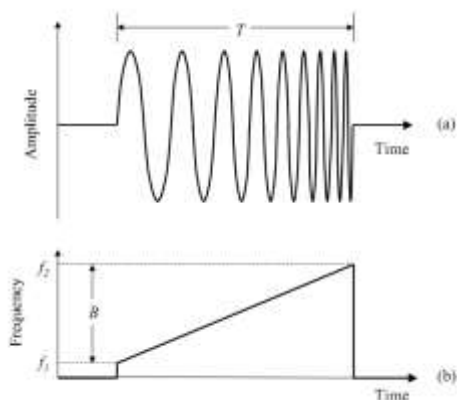


Figure 2. The amplitude of (a) a frequency-modulated pulse over time and (b) the frequency of the same pulse over time.

Figure 2(a) illustrates the instantaneous frequency of LFM waveform that sweeps from f_0 to f_1 . The characteristic of interest in Figure 2(b) is the bandwidth of the modulation within the pulse, B . The bandwidth is simply the difference between the highest and lowest frequencies within the uncompressed pulse.

To recognize the presence of the uncompressed pulse, the pulse-compression filter performs a correlation between the received pulse and the transmitted pulse. The pulse-compression filter (matched filter) is simply looking for a strong correlation between what was transmitted and what was received.

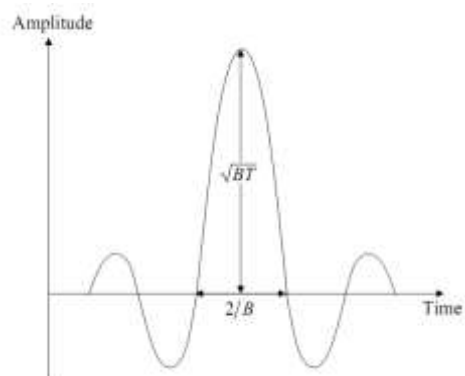


Figure 3. Typical output from a pulse-compression filter

The output of the pulse-compression filter forms the input into the detector section of the pulse-compression radar. It is therefore desirable to have a very narrow and tall pulse. The main points in Figure 3 are that the input to the filter is a relatively wide and low- power pulse. The output pulse, however, is very narrow and strong; two very desirable characteristics from a pulse radar.

The output of the pulse-compression filter shown in Figure 3 represents the amplitude of a signal rather than its power. To be consistent with the radar range equation, the output of the pulse-compression filter is converted into power that is taken as the square of the amplitude. When the signal in Figure 3 is converted into power, the peak value of the pulse becomes the product of the modulation bandwidth, B and the uncompressed pulse width, T . This is known as the pulse-compression ratio of the pulse-compression radar.

$$\text{Pulse compression ratio} = B \times T \quad (6)$$

where B is the bandwidth of the modulation within each pulse in hertz and T is the uncompressed pulse width in seconds.

The width of the compressed pulse is simply the inverse of the modulation bandwidth, B.
 Compressed pulse width = $1/B$ (7)
 where B is the bandwidth of the modulation within each pulse in hertz.

2.2 Matched Filter

In radar applications the reflected signal is used to determine the existence of the target. The reflected signal is corrupted by additive white Gaussian noise (AWGN). The probability of detection is related to signal-to-noise ratio (SNR) rather than exact shape of the signal received. Hence it is required to maximize the SNR rather than preserving the shape of the signal. A filter which maximizes the output SNR is called matched filter [5].

Pulse compression radar is the practical implementation of a matched-filter system. The coded signal can be described either by the frequency response $H(\omega)$ or as an impulse response $h(t)$ of the coding filter. The received echo is fed into a matched filter whose frequency response is the complex conjugate $H^*(\omega)$ of the coding filter. The output of the matched filter, $y(t)$ is the compressed pulse which is just the inverse Fourier transform of the product of the signal spectrum and the matched filter Response.

$$y(t) = \frac{1}{2\pi} \int_{-\infty}^{\infty} |H(\omega)|^2 \exp(j\omega x) d\omega \quad (8)$$

A filter is also matched if the signal is the complex conjugate of the time inverse of the filter's impulse-response. This is often achieved by applying the time inverse of the received signal to the pulse-compression filter. The output of this matched filter is given by the convolution of the signal $h(t)$ with the conjugate impulse response $h^*(t)$ of the matched filter

$$y(t) = \int_{-\infty}^{\infty} h(\tau) h^*(t - \tau) d\tau \quad (9)$$

3. SIMULATION RESULTS

Firstly, for the testing purpose of simulation certain LFM pulse waveform is generated with the following characteristics:

- Sample rate= $1e6$
- Duration of a single pulse= $100e-6$
- Pulse repetition frequency= $5e3$
- Sweep bandwidth $1e5$
- Sweep direction=up

The parameters are defined based on the specifications of some radar simulation project. Figure 4 shows an uncompressed chirp pulse representing the transmitted pulse. Noise and attenuation are a real problem when operating radar systems, so both random noise and signal attenuation are incorporated, and is shown in Figure 5. The output of the corresponding pulse-compression filter is shown in Figure 6 when that pulse is processed.

The two graphs in Figure 4 and Figure 6 are drawn on the same time scale (horizontal axis) to show how the process has compressed into a very narrow pulse. It is not possible to draw the amplitude axes (vertical axis) on the same scale due to the magnitude difference between Figure 4 and 6. The amplitude of the pulse in Figure 6 is approximately 100 times larger than Figure 4. Although the noise effects on the input pulse, the output is still impressive from a peak amplitude and pulse-width perspective and the target is clearly visible.

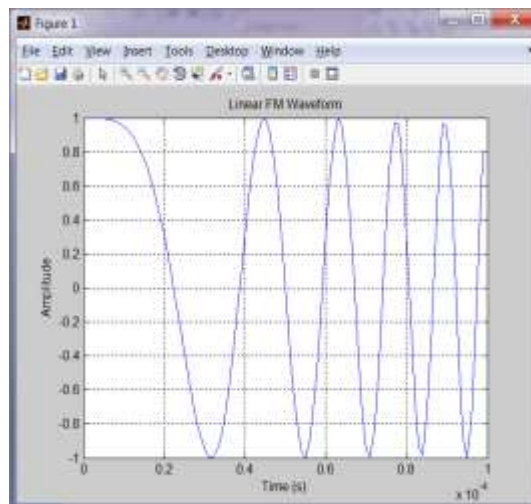


Figure 4. LFM Uncompress Pulse

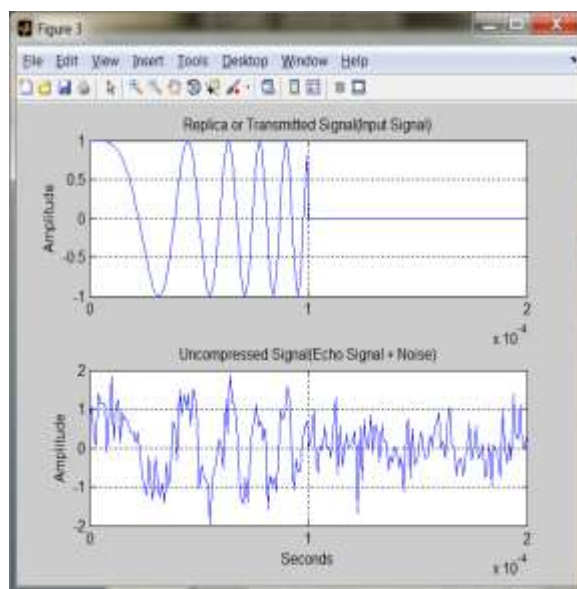


Figure 5. LFM Uncompress Pulse and Noise Signal

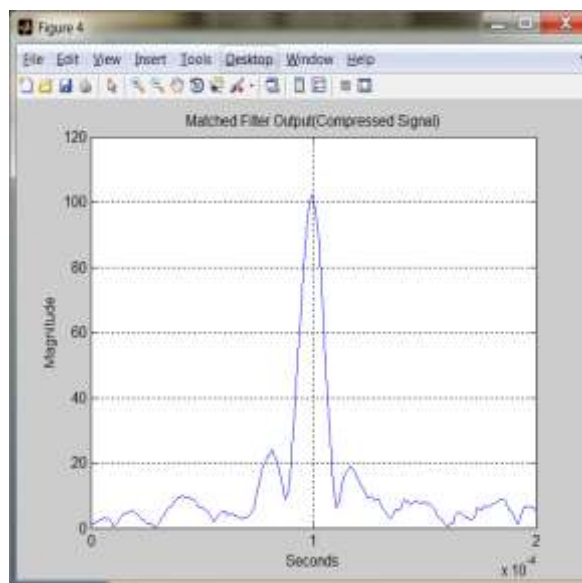


Figure 6. Compressed Pulse

Secondly, the linear FM waveform is configured with the following characteristics. The desired range resolution determines the waveform bandwidth. For a linear FM waveform, the bandwidth is equal to its sweep bandwidth. However, the pulse width is no longer restricted to the reciprocal of the pulse bandwidth, so a much longer pulse width can be used. We use a pulse width that is 20 times longer and set the sample rate to be twice the pulse bandwidth.

The input parameters for the simulation are
 Number of targets within the radar's maximum range = 3
 Radar's maximum range = 6000 m
 Range Resolution = 50;
 Chirp bandwidth = $c/(2 * \text{range_res}) = 30\text{MHz}$
 Uncompressed Pulse Width (seconds) = $20/\text{BW}$;
 Sampling Frequency = $2 * \text{BW}$;
 Targets' relative range (m) = 2000, 3500, 3600

Figure 7 illustrates the created LFM waveform. Figure 8 is simulation result of uncompressed echo in time domain (seconds). Scatters are not resolved. Figure 9 illustrates the compressed echo signal in target position (meters). Two targets that are located at long range with very small separation (100 meters) between them are resolved.

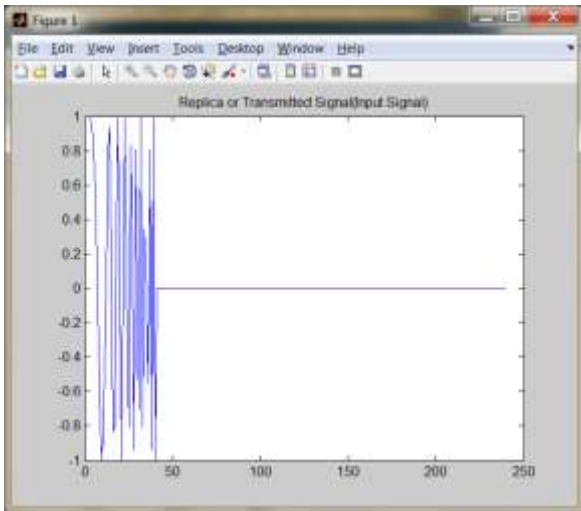


Figure 7. Transmitted LFM pulse

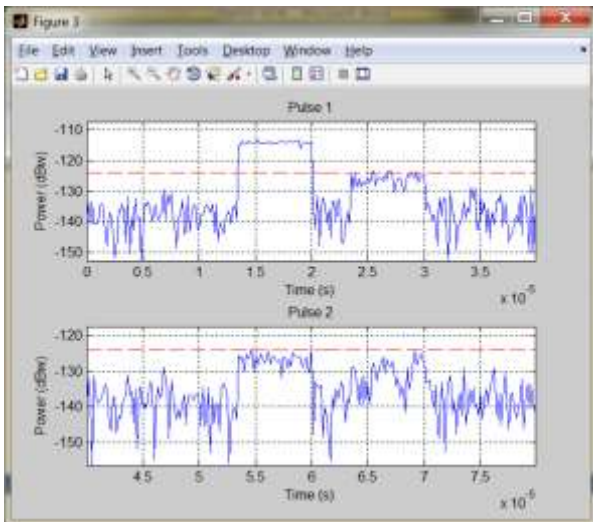


Figure 8. Received signal (Uncompressed echo)

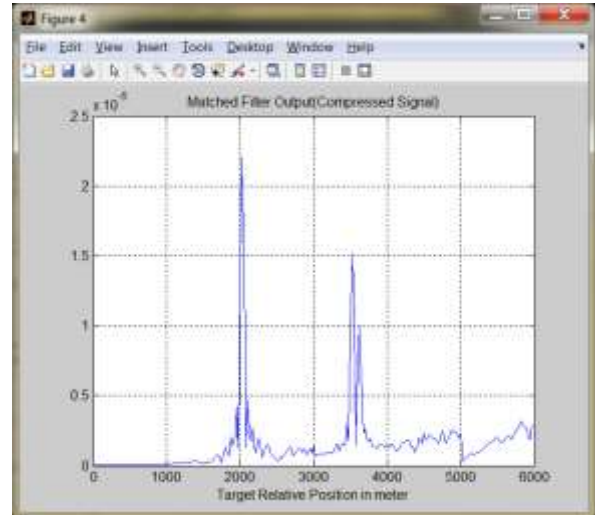


Figure 9. Compressed echo

And then, the program is simulated by setting the two targets in the range 3500 and 3560 meters. When two targets are separated by 60 meters, it can resolve completely as shown in Figure 10.

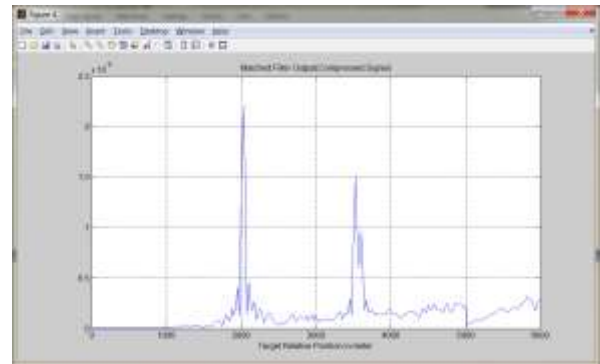


Figure 10. Compressed echo

Figure 11 is similar to Figure 10 except in this case the second and third targets are less than range resolution apart (They are at 3500 and 3540 meters from radar)

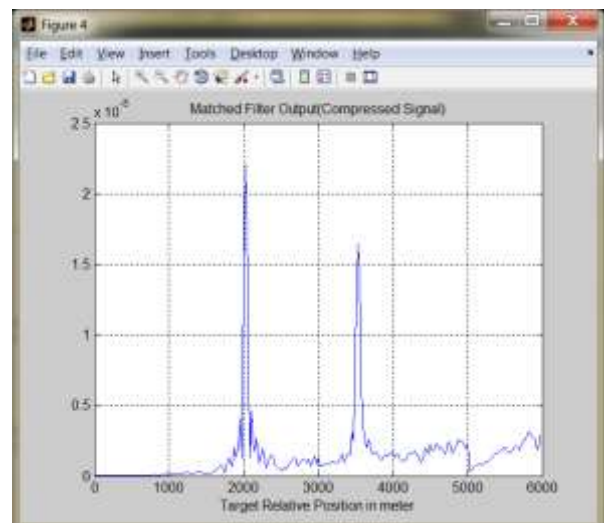


Figure 11. Compressed echo of two unresolved targets

4. CONCLUSIONS

The concept of pulse-compression was presented in this paper using the linear FM (or chirp) pulse modulation. In this method, received signal is compared to matched filter impulse response for correlation. A compression of the effective pulse width of received pulses leading to range advantages and range resolution improvements. The effectiveness of pulse-compression is determined by the width of the uncompressed pulse and the bandwidth of the modulation within the uncompressed pulse. The most impressive results come from broad uncompressed pulse widths containing a modulated pulse with a large bandwidth. Range resolution is the ability to separate multiple targets at different ranges. To be resolved in range, the basic criterion is that targets must be separated at least in the range equivalent of the width of the processed echo pulse. In this paper, it is shown that the distance between two targets less than range resolution and the targets are not resolved.

5. REFERENCES

- [1] Skolnik, M.I., Introduction to Radar Systems, Sydney: McGraw-Hill, 1988, p. 434.
- [2] D.K. Barton, Pulse Compression. Artech House, 1975.
- [3] A.W. Rihaczek, Principle of high resolution radar. McGraw Hill, New York, 1969.
- [4] Stimson, G.W., Introduction to Airborne Radar, New Jersey: SciTech Publishing Inc., 1998, p. 393.
- [5] Jane's Radar and Electronic Warfare Systems 1999-00, AN/APS- 134(V)/-134 (Plus) Maritime Surveillance Radars, Jane's Information Group, 1999.
- [6] B. L. Lewis, F. F. Kretschmer Jr., "Linear Frequency Modulation Derived Polyphase Pulse Compression Codes", IEEE Trans. on Aerospace and Electronic Systems, vol. AES-18, no. 5, pp. 637-641, Sep. 1982.
- [7] F.E. Nathanson, J. P. Reilly and M. N. Cohen, "Radar Design Principles Signal Processing and the Environment", 2nd ed. New York: McGraw-Hill, 1999, chapt. 1 & 8.